

A Multi-scale Approach for Simulations of Kelvin Probe Force Microscopy with Atomic Resolution

Ali Sadeghi, Alexis Baratoff, S. Alireza Ghasemi, Stefan Goedecker, Thilo Glatzel, Shigeki Kawai and Ernst Meyer
Department of Physics, University of Basel, Klingelbergstrasse 82, CH-4056 Basel, Switzerland

(Dated: August 31, 2018)

The distance dependence and atomic-scale contrast recently observed in nominal contact potential difference (CPD) signals simultaneously recorded by KPFM using non-contact atomic force microscopy (NCAFM) on defect-free surfaces of insulating, as well as semiconducting samples, have stimulated theoretical attempts to explain such effects. Especially in the case of insulators, it is not quite clear how the applied bias voltage affects electrostatic forces acting on the atomic scale. We attack this problem in two steps. First, the electrostatics of the macroscopic tip-cantilever-sample system is treated by a finite-difference method on an adjustable nonuniform mesh. Then the resulting electric field under the tip apex is inserted into a series of atomistic wavelet-based density functional theory (DFT) calculations. Results are shown for a realistic neutral but reactive silicon nano-scale tip interacting with a NaCl(001) sample. Bias-dependent forces and resulting atomic displacements are computed to within an unprecedented accuracy. Theoretical expressions for amplitude modulation (AM) and frequency modulation (FM) KPFM signals and for the corresponding local contact potential differences (LCPD) are obtained by combining the macroscopic and atomistic contributions to the electrostatic force component generated at the voltage modulation frequency, and evaluated for several tip oscillation amplitudes A up to 10 nm. For $A = 0.1 \text{ \AA}$, the computed LCPD contrast is proportional to the slope of the atomistic force versus bias in the AM mode and to its derivative with respect to the tip-sample separation in the FM mode. Being essentially constant over a few Volts, this slope is the basic quantity which determines variations of the atomic-scale LCPD contrast. Already above $A = 1 \text{ \AA}$, the LCPD contrasts in both modes exhibit almost the same spatial dependence as the slope. In the AM mode, this contrast is approximately proportional to $A^{-1/2}$, but remains much weaker than the contrast in the FM mode, which drops somewhat faster as A is increased. These trends are a consequence of the macroscopic contributions to the KPFM signal, which are stronger in the AM-mode and especially important if the sample is an insulator even at sub-nanometer separations where atomic-scale contrast appears.

PACS numbers: 68.37.Ps, 07.79.Lh, 02.70.Bf, 31.15.A-

I. INTRODUCTION

Kelvin probe force microscopy (KPFM), which was introduced twenty years ago,^{1,2} has become an attractive non-contact technique to determine the electric surface characteristics of materials. Among many applications, this technique has been successfully applied for mapping local work function or surface potential variations along inhomogeneous surfaces of various materials.³⁻⁵ For a conducting crystal, the work function corresponds to the energy difference between the vacuum level outside the surface at a distance large compared to the lattice spacing, yet small compared to the lateral dimensions of a homogeneous patch, and the bulk Fermi level. In this range, which is typical for conventional KPFM measurements, the potential acting on an electron approaches the local vacuum level and becomes constant, except in the vicinity of surface steps or patch boundaries. Differences between local vacuum levels are solely due to electrostatic contributions which give rise to fringing electric fields around such boundaries. If the sample is covered by a thin overlayer of foreign material, the work function can change owing to electron transfer and structural relaxation at the interface.⁶ Similar changes can occur at the surface of a doped semiconductor, owing to band bending in a subsurface depletion layer. As long as elec-

trochemical equilibrium occurs the Fermi level is aligned throughout the sample and with the Fermi level of the back-electrode. However, if the sample is a wide-bandgap insulator, e.g. an alkali halide crystal, this equilibration may require very long times, so that the bulk Fermi level is not well-defined. Charge rearrangements and relaxation occur at the interface with the back electrode and cause an additive shift of the local vacuum level outside the surface with respect to the Fermi level of the back electrode. In a real, thick enough insulator with charged impurities, such a shift will also be affected by the distribution of spatially separated charged defects at the interface, the surface and in the bulk of the sample, as well as by their slow diffusion over time^{4,7}.

When two separated conducting bodies, e.g. the probe tip of an *Atomic Force Microscope* (AFM) and the sample, with different work functions ϕ_t and ϕ_s are connected via back electrodes, electrons are transferred until the Fermi levels become aligned. The charged bodies then develop a *contact potential difference* (CPD), of $V_{CPD} = (\phi_t - \phi_s)/e$, where e is the elementary charge and the sample is grounded. If the tip is biased at V_b with respect to the sample, a finite electric field $\mathbf{E} \propto V$ develops in the gap between them and causes an attractive electrostatic force proportional to V^2 where $V = V_b - V_{CPD}$ is their *effective potential difference*. If the sample is an

insulator the same phenomenon occurs, but ϕ_s must be referred to the Fermi level of the back-electrode and is therefore affected by all the above-mentioned shifts, and so is V_{CPD} . It is then more appropriate to focus attention on variations of V_{CPD} along the surface rather than on its absolute value which is affected by sample preparation.

In KPFM, a signal determined by this electrostatic force is compensated by applying a DC bias $V_b = V_{CPD}$. For fast measurements the applied bias consists of an AC modulation voltage with angular frequency $\omega = 2\pi f$ in addition to the DC voltage:

$$V_b(t) = V_{DC} + V_{AC} \cos \omega t. \quad (1)$$

Assuming that the electric response is linear and in-phase with V_{AC} , the electrostatic force acting on the tip can be decomposed into three spectral components:

$$F(t) = F_{DC} + F_\omega \cos \omega t + F_{2\omega} \cos 2\omega t. \quad (2)$$

The ω component of the KPFM signal, which is proportional to $(V_{DC} - V_{CPD}) V_{AC}$, is selectively detected by a lock-in amplifier and compensated by a feedback circuit.

CPD variations along a surface can be conveniently measured together with its topography,² as determined by *non-contact atomic force microscopy* (NCAFM). In most state-of-the-art NCAFM experiments a micro-fabricated cantilever with a tip at its free end (typically etched out of doped single-crystal silicon) oscillates with a constant amplitude A at the frequency f_1 of a flexural resonance (usually the fundamental mode).^{8,9} Distance-dependent tip-sample forces cause a frequency shift Δf_1 which can be very accurately measured using FM detection (frequency demodulation)¹⁰ and used for distance control. In *combined NCAFM-KPFM*, the F_ω component is simultaneously sensed; either the modulated deflection signal (*Amplitude Modulation* KPFM¹¹) or the modulation of the resonance frequency shift Δf_1 (*Frequency Modulation* KPFM¹²) is actually detected.^{13,14} In either case the amplitude of the signal at the modulation frequency f is proportional to $(V_{DC} - V_{CPD})V_{AC}$. Thus V_{CPD} can be recorded by continuously adjusting V_{DC} so that the modulation signal vanishes while scanning the tip parallel to the sample surface at a distance controlled by the (non-modulated) shift Δf_1 .⁹ Both modulation techniques are much faster and more sensitive than the direct method in which V_{CPD} is determined from the extremum of the parabolic $\Delta f_1(V_b)$ curve measured by slowly sweeping V_b at each measurement point.^{15–18} Potential artifacts of the modulation techniques¹⁹ are avoided in the direct quasistatic method. Because the scope of this article is primarily theoretical, we don't further consider such experimental difficulties, but focus our attention on still controversial *atomic-scale variations* of the so-called *local* CPD or V_{LCPD} on large defect-free surface areas. Thus we deliberately leave out local changes due to charged surface defects^{4,17,20} or adsorbates^{18,21} which have recently attracted considerable attention, also in theory.^{22,23}

Atomic-scale variations of Δf_1 can be detected by NCAFM on well-prepared surfaces in ultrahigh vacuum if the closest approach distance of the tip is smaller than the lattice spacing or the spacing between protruding atoms.⁸ The contrast in Δf_1 then arises from short-range interatomic forces which begin to act in that distance range, while cantilever jump-to-contact is avoided if the total force remains much smaller than the maximum restoring force kA , k and A being respectively the flexural lever stiffness and oscillation amplitude.⁹ Combined NCAFM-KPFM experiments have proven that FM-KPFM,^{16,24–27} as well as AM-KPFM^{28–30} could detect lateral atomic-scale variations of V_{LCPD} in the range where Δf_1 exhibits similar variations on surfaces of semiconductors, as well as of ionic crystals. Understanding the connections between the observed contrast in V_{LCPD} and the atomic-scale variations of the electrostatic potential just outside the surface has been a challenging task, especially on unreconstructed cleavage faces of rocksalt-type crystals.²⁹ Above a flat homogeneous surface V_{LCPD} must, in principle, approach the corresponding V_{CPD} at somewhat larger tip-sample separations. In practice, however, this ideal behavior is often masked by a slow dependence caused by the finite lateral resolution of surface inhomogeneities, e.g. finite islands of materials with different work functions. This effect is less pronounced in FM- than in AM-KPFM.^{13,27,31,32} Several researchers developed models and computational schemes based on classical electrostatics which treated the tip and the sample (sometimes also the cantilever) as macroscopic bodies in order to interpret the resolution of KPFM images of inhomogeneous surfaces on lateral scales of several nanometers and above.^{33–40} On the other hand, only few authors considered atomistic nano-scale tip-sample systems, either neglecting^{16,41} or including the macroscopic contributions via simple approximations. In the first theoretical study of combined NCAFM-KPFM on an ionic crystal sample,^{5,29,42} a formally correct partitioning was proposed between capacitive and short-range electrostatic forces induced by the effective macroscopic bias V . This analytic treatment also provided qualitative insights into the origin of atomic-scale *LCPD* contrast, although underestimating the capacitive forces caused a quantitatively disagreement with experimental results as will be explained in subsection III A. More reliable results were obtained for a NaCl(001) sample interacting with a model tip consisting of a conducting sphere terminated by a NaCl cluster by allowing local atomic deformations.⁴³ These atomistic simulations were based on the SCIFI code⁴⁴ which has provided detailed insights into NCAFM on ionic compounds.^{45,46}

In the present work, which is based on separate classical electrostatics and *ab initio* calculations, we propose a more rigorous and accurate approach for coupling interactions acting on widely different length scales which leads to an unambiguous definition of V_{LCPD} . The outline of this paper is as follows: in Section II we discuss previous approaches, then present our own computation-

ally simple, yet flexible finite-difference (FD) scheme with controlled accuracy to treat electrostatic tip-sample interactions on macro- and mesoscopic scales. Owing to electric field penetration into the dielectric sample, the tip shank and the cantilever significantly affect the capacitive force and its gradient even at sub-nanometer tip-surface separations where atomic-scale contrast appears. We also explain how the influence of the effective bias V can be included into atomistic calculations, as well as shortcomings of previous attempts to do so. In Section III we critically discuss previous atomistic calculations, as well as experimental evidence for short-range electrostatic interactions. Density functional calculations for nano-scale tip-sample systems are then discussed and illustrated for a realistic Si tip close to a NaCl(001) slab as an example of current interest. One important result is that the microscopic short-range force is proportional to V over a few volts; the corresponding slope is thus the basic quantity that should be extracted from KPFM measurements. In Section IV expressions for V_{LCPD} in AM- and FM-KPFM are obtained and evaluated, first for ultrasmall, then for finite tip oscillation amplitude A . Their magnitude and dependence on A are explained in detail in terms of the above-mentioned macroscopic contributions to the capacitive force. Experimental limitations and evidence for the predicted trends, as well as desirable measurements are also briefly discussed. Finally, in Section V the main features of our approach and of our results are summarized, and conclusions are drawn.

II. MACROSCOPIC ELECTROSTATIC INTERACTION

A. Previous approaches

Calculating the cantilever-tip-sample electrostatic interaction is, in fact, an intricate electrostatic boundary-value problem. The main difficulty is due to the presence of several length scales determined by the nontrivial shape of AFM components, as well as to the distance-dependent redistribution of the surface charge density at constant bias voltage. In the case of conductive bodies with cylindrical symmetry, a simple assumption (uniform electric field along field lines approximated by circular arcs to their surfaces) led to an analytic expression for the force on the tip treated as cone with a spherical end cap.⁴⁷ Recent numerical calculations^{22,48} showed that Hudlet's expression is surprisingly accurate. Somewhat different analytical expressions and estimates for the lateral resolution in AM- and FM-KPFM were obtained for similar probes, also including a tilted cantilever.³⁶ For cylindrical geometries, many authors proposed numerical schemes based on the image charge method which is applicable to simple geometries involving spherical and planar surfaces.⁴⁹ Thus Belaidi *et al*⁵⁰ placed N point charges on the symmetry axis and determined their po-

sitions and strengths by forcing the potential on the tip surface to be V by a nonlinear least squares fit. The previously mentioned authors also described how contributions of the spherical cap, the tip shank and the cantilever to the macroscopic force lead to characteristic distance dependencies on scales determined by the geometry and dimensions of those parts. A *linearized* version of the *numerical image charge method* where the positions of axial point and line charges were fixed was applied to study tip-shape effects for conductive and *dielectric samples*^{37,51} and *thin films on conducting substrates*⁵², also including the influence of the cantilever⁵³. It is not known to what extent the boundary conditions must be satisfied for a given accuracy in the numerical image method, unlike in the analytic method where the positions and strengths of the image charges change with tip-sample separation and the boundary conditions are fully satisfied (see Appendix B).

A more systematic approach to multi-length-scale problems is the *boundary element method* (BEM)^{38,39,48}. In this method the 3D (2D) differential Poisson's equation is transformed into 2D (1D) integral (Green's functions) equations on the surfaces of conductive or dielectric components, including CPD discontinuities and surface charges if desired.⁴⁰ The accuracy of BEM is controlled by the mesh resolution and is applicable to complex probe-sample systems, e.g. including a realistic cantilever⁵⁴. The size of the resulting linear system of equations is small compared to volumetric discretization methods. However, because of the memory requirement of $\mathcal{O}(N^2)$ to store the fully populated matrix and complexity of $\mathcal{O}(N^3)$ to solve the linear equations, BEM has mostly been applied to systems with a relatively small number N of grid points, e.g. problems of high symmetry and homogeneity for which it is feasible to derive the Green's function analytically. Somewhat earlier a few authors adapted Green's function methods developed for more complex near-field optics problems to investigate lateral resolution in KPFM on inhomogeneous samples^{34,37}. One advantage of BEM is that the LCPD of such samples can be expressed as a 2D convolution of the CPD and/or of a fixed surface charge distribution with a point-spread function which depends only on the relative position of the scanning probe.^{38,48,54} The distance-dependent lateral resolution can be quantified by the width of that function. Moreover, if one assumes that only one of those distribution is present, its can be determined by inversion of the BEM matrix upon discretization on the adjustable BEM mesh.⁴⁰

Conceptually more straightforward approaches involving surface elements have been applied to conductive probe and sample systems. In the simplest one, the tip surface is approximated as a regular staircase (or, equivalently, as an *array of capacitors in parallel*),^{13,34,55}. More accurate methods rely on adjustable meshes. Thus the *finite element method* (FEM) was used to calculate the electrostatic force acting on a conical tip,³⁵ while a commercial FEM software was recently applied to sim-

ulate a realistic cantilever and tip of actual shape and dimensions over a *conducting* flat sample with a CPD discontinuity.⁵⁶ More sophisticated software packages have been used to solve the Poisson's equation in the presence of space charges, e.g. for structured samples involving doped semiconductors^{33,57}. Numerical methods which involve 3D discretization require a very large number of grid points even if the mesh is carefully adjusted; the computational box must therefore be truncated at some finite extent.

B. Implementation of finite-difference method

As an alternative we present a finite-difference method (FDM) on a 3D non-uniform grid which is capable of dealing with realistic sizes of the cantilever, tip and sample. Inhomogeneous metallic and dielectric samples as well as thin dielectric films on metal substrates, can be straightforwardly treated with this method. The most attractive feature of our FDM compared to FEM or BEM computations is its ease of implementation. Since the electrostatic potential varies smoothly and slowly at distances far from the tip apex, we use a grid spacing which increases exponentially away from this region. Consequently, the number of grid points depends logarithmically on the truncation lengths, and an extension of the computational box costs relatively few additional grid points. It allows us to simulate the cantilever as well as thick dielectric samples according to their actual sizes in experiments.

The capacitance $C(s)$ between the probe and the sample back-electrode depends only on the tip-sample separation s , provided that their geometries are fixed.⁵⁸ The macroscopic electrostatic energy due to the effective voltage difference $V = V_b - V_{CPD}$ between the conducting tip and back-electrode is given by $U_c(s, V) = \frac{1}{2}C(s)V^2$. The electrostatic force exerted on the tip is proportional to the capacitance-gradient $C'(s)$

$$F_M(s, V) = -\frac{\partial U}{\partial s} = + \left(\frac{\partial U_c}{\partial s} \right)_V = +\frac{1}{2}C'(s)V^2. \quad (3)$$

Similarly, the force-gradient is proportional to $C''(s) = \partial^2 C / \partial s^2$. We wish to emphasize the difference between U and U_c which leads to the positive sign on the RHS of Eq. (3); the reason is restated for convenience in Appendix A. The electrostatic energy

$$U_c(s, V) = \frac{1}{2} \int \epsilon(\mathbf{r}) |\nabla \Phi|^2 d\mathbf{r}$$

can be determined once the electrostatic potential $\Phi(\mathbf{r}; s, V)$ is known at any point \mathbf{r} in space. In general, when the dielectric constant $\epsilon(\mathbf{r})$ varies in space, Φ satisfies the generalized form of Poisson's equation

$$\nabla \cdot [\epsilon(\mathbf{r}) \nabla \Phi(\mathbf{r})] = -\rho(\mathbf{r}), \quad (4)$$

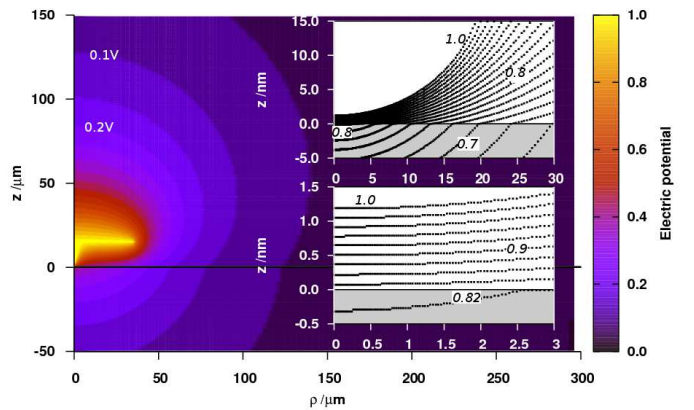


FIG. 1. (color online) 2D (ρ, z) maps of the macroscopic electrostatic potential at three magnifications ($\times 10^4$ and $\times 10^5$ in zoom-in windows). An effective bias $V = 1$ Volt is applied to the conducting probe while the back-electrode as well as the surrounding enclosure are grounded. The yellow region corresponding to $\Phi = 1V$ reflects the assumed cylindrically symmetric probe geometry: a cone with 15° half-angle terminated by a spherical cap of radius $R = 20$ nm. The cone is 15nm high and attached to a disk of thickness $0.5 \mu\text{m}$. The radius of the disk is $35 \mu\text{m}$ which matches the area of a typical cantilever. The sample is a 1-mm thick dielectric slab with the relative permittivity $\epsilon/\epsilon_0 = 5.9$ of NaCl. The back electrode and the surrounding enclosure of height and radius $10^6 R = 20$ mm are grounded (not shown). The sample-vacuum interface is indicated by the horizontal lines at $z = 0$.

ρ being the charge density. Minimization of the energy-like functional

$$I[\Psi(\mathbf{r})] = \frac{1}{2} \int \epsilon(\mathbf{r}) |\nabla \Psi|^2 d\mathbf{r} - \int \rho \Psi d\mathbf{r}. \quad (5)$$

subject to Dirichlet boundary conditions leads to Φ , the solution of the Poisson's equation Eq.(4) with the same boundary conditions.⁴⁹ Using a discretized variational approach, we therefore minimize the functional

$$I(\{\Psi_{\mathbf{n}}\}) = \sum_{\mathbf{n}} \left(\frac{1}{2} \epsilon_{\mathbf{n}} |\nabla \Psi_{\mathbf{n}}|^2 - \rho_{\mathbf{n}} \Psi_{\mathbf{n}} \right) v_{\mathbf{n}}. \quad (6)$$

On a non-uniform grid, we delimit the volume $v_{\mathbf{n}}$ of the volume element assigned to node \mathbf{n} by neighboring nodes. Then, $\Psi_{\mathbf{n}}$, $\rho_{\mathbf{n}}$, $\epsilon_{\mathbf{n}}$ and the electric field $-\nabla \Psi_{\mathbf{n}}$ are *evaluated at the center of the volume element* by linear interpolation between the nodes adjacent to \mathbf{n} in orthogonal directions. This ensures that the field is effectively evaluated to second order in the product of grid spacings and that discontinuities in $\nabla \Psi_{\mathbf{n}}$ and $\epsilon_{\mathbf{n}}$ at material interfaces are correctly treated. Although the formalism is general and can be applied to any 3D system on a judiciously chosen nonuniform 3D orthogonal grid, in the following examples we *consider a cylindrically symmetric setup without free charges* in order to allow comparison with most previous computations. In cylindrical coordinates, each volume element is a truncated tube of

height $h_k^{(z)}$ with inner and outer radii ρ_i , ρ_{i+1} , respectively, and $v_{\mathbf{n}} = \pi(\rho_{i+1} + \rho_i)h_i^{(\rho)}h_k^{(z)}$, $h_i^{(\rho)} = \rho_{i+1} - \rho_i$ and $h_k^{(z)} = z_{k+1} - z_k$ being respectively the radial and vertical spacings of the appropriate nonuniform grid. The radial and vertical components of $\nabla\Psi$ are approximated on the circle of radius $\rho_i + 0.5h_i^{(\rho)}$ at $z_k + 0.5h_k^{(z)}$ as $(\Psi_{i+1,k} - \Psi_{i,k})/h_i^{(\rho)}$ and $(\Psi_{i,k+1} - \Psi_{i,k})/h_k^{(z)}$. Since the FD approximation of the electric field is a linear combination of the potential values on nearest neighbor nodes, the functional in Eq. (6) is quadratic and the minimization condition $\partial I/\partial\Psi_{\mathbf{n}} = 0$ yields a system of *linear* equations $A\Phi = \mathbf{b}$ where the vector \mathbf{b} describes imposed boundary values and charge distributions. Because A is a sparse, symmetric and block-tridiagonal matrix, the system can be solved efficiently by an iterative procedure, which may, however, suffer from conditioning problems due to the nonuniformity of the grid. For an accurate solution, a mesh with high enough resolution is required in regions where $\Phi(\mathbf{r}; s, V)$ varies strongly. We used the PARDISO package⁵⁹ to solve the resulting huge system of equations. An implementation of our FDM is distributed under GNU-GPL license as the CapSol code⁶⁰.

Once $\Phi(\mathbf{r}, s, V=1)$ is determined for several separations s , the system capacitance is obtained as $C(s) = \int \epsilon(\mathbf{r})|\nabla\Phi|^2 d\mathbf{r} \simeq \sum_{\mathbf{n}} \epsilon_{\mathbf{n}} |\nabla\Phi|_{\mathbf{n}}^2 v_{\mathbf{n}}$. Then a simple second order FD approximation is used to evaluate $C'(s)$ and $C''(s)$ from $C(s)$. The electrostatic force acting on an arbitrary area S of a conducting part can also be evaluated as

$$\mathbf{F}_S = \frac{1}{2\epsilon_0} \int_S \sigma(s)^2 \hat{n} dS, \quad (7)$$

where $\sigma(s) = -\epsilon\partial\Phi/\partial n$ is the surface charge density guaranteeing that the tip surface is an equipotential, and \hat{n} is the unit vector normal to the surface element dS . For a system with cylindrical symmetry the net force on a part of the probe delimited by two cylinders of radii $\rho_1 < \rho_2$ is vertical and given by $F = \pi\epsilon_0 \int_{\rho_1}^{\rho_2} |\nabla\Phi|^2 \rho d\rho$, however we prefer to use Eq. (3) to calculate the total macroscopic force on the probe. In the following subsections we validate the performance of our FDM by comparisons with previous results obtained by other methods for cylindrically symmetric systems. We mainly consider the macroscopic model system described in the caption of Fig. 1 which shows 2D (ρ, z) maps of the electrostatic potential computed by our FDM at three magnifications differing by five orders. The conducting probe consists of a conical tip terminated by a spherical cap of radius R attached to a cantilever modelled as a disk of the same area as a typical cantilever,³⁴ and the sample by a thick dielectric slab. Dirichlet boundary conditions are applied on a very large cylindrical box. Note that the grid spacing changes by six orders of magnitude (hundredths of nm around the tip apex to tens of μm near the box walls). The indented contours in the bottom right inset reveal the resolution of the finest grid, i.e. 0.02 nm. The contours in both magnified insets clearly show that for a

separation of 1 nm a large fraction of the voltage drop occurs within the dielectric sample. Whereas the contour spacing between the tip apex and the surface is constant to a good approximation, it gradually increases inside the dielectric, in contrast to what occurs in a parallel plate capacitor. Actually the capacitance remains finite for an infinitely thick sample even in the (macroscopic) contact limit $s \rightarrow 0$ (see Appendix B).

C. Convergence and Accuracy

Grid spacing: We first test our implementation for the problem of a conducting sphere of radius R separated by s from a semi-infinite dielectric surface for which an analytic solution of controllable accuracy is available (see Appendix B). A convergence analysis yields the parameters needed to achieve a desired accuracy. Compared to the analytic solution, the convergence with respect to the finest grid spacing h_0 of the sphere-dielectric system (Fig. 2) shows a nearly quadratic error scaling for small separations as expected for a second order FDM. The accuracy could be improved by using a higher order approximation for the electric field over further neighboring points. However, a corresponding improvement of the approximation of curved surfaces on the orthogonal FD-mesh is then also required. Note that, for consistency, the surface of the sphere must be approximated as a staircase with variable step heights and widths which also change when the grid-spacing is changed. Thus the error scaling deviates somewhat from the ideal straight line and is no longer quadratic when the separation increases. The capacitance, force and force-gradient of this test system at a rather small separation of $s = R/20$ can be calculated within a relative error of 0.005 compared to the analytic solution if $h_0 = R/100$. For larger separations, this accuracy is achieved even with a larger h_0 .

For the cantilever-tip-sample system shown in Fig. 1 and the results in the next subsection, a uniform grid with $h^{(\rho)} = h^{(z)} = h_0 = R/100$ is used around the tip apex up to a distance of twice the tip apex radius in both radial and vertical directions. Outside this range the grid becomes gradually coarser with a growth factor of 1.01. In order to consistently preserve the shape of the tip approximated by the orthogonal mesh, the tip-sample separation must be changed in steps of h_0 .

Space truncation: A convergence analysis with respect to the size of the computational cylinder is shown in Fig. 3 for the model system described in Fig. 1. The capacitance approaches the same asymptotic value when the truncation length in a particular direction is increased while the other one is kept fixed and sufficiently large. If the computational box extends to $10^6 R$ in the radial and vertical directions, the relative deviation of the capacitance from its asymptotic value is only 10^{-7} (as indicated by the arrow in Fig. 3). We use these cutoff parameters in all subsequent FDM computations reported here.

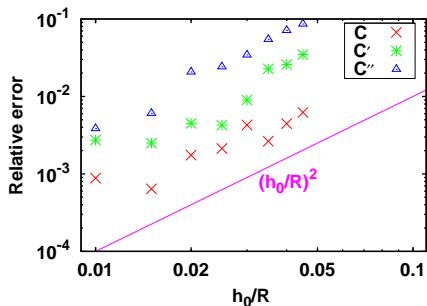


FIG. 2. (color online) Convergence analysis with respect to the finest grid spacing h_0 for a conducting sphere of radius R in front of a 1 mm thick dielectric of relative permittivity $\epsilon/\epsilon_0 = 5.9$. Points computed by our FDM for the macroscopic capacitance C , the force $\propto C'$ and force gradient $\propto C''$ are compared to the analytic solution for a semi-infinite dielectric described in Appendix B. The sphere-surface separation is $R/20$ and the computational box extends to $10^6 R$ in the radial and vertical directions. The straight line in the log-log plot indicates the expected quadratic error scaling.

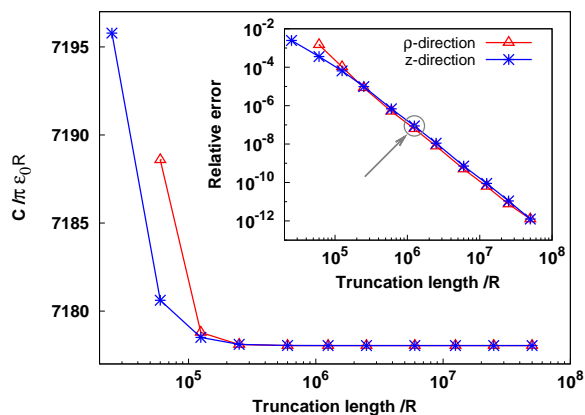


FIG. 3. (color online) Convergence analysis with respect to the radial and vertical extents of the FDM computational box for the macroscopic system described in the caption of Fig. 1, the tip-sample separation and finest mesh size being $s = R/20$ and $h_0 = R/100$, respectively. The normalized capacitance of the system approaches the same asymptotic value upon increasing the truncation length in one direction while the other one is sufficiently large and fixed. Relative deviations with respect to the asymptotic value are shown in the inset. The arrow indicates the truncation length adopted in subsequent FDM computations.

Comparison: In Fig. 4 we compare results obtained by our FDM with previous accurate BEM computations⁴⁸ for a system like in Fig. 1 but *without the cantilever* for a conducting and a dielectric ($\epsilon/\epsilon_0 = 40$) sample. The force and the force-gradient evaluated by the two methods are in very good agreement for both kinds of samples. For the conducting sample, Hudlet's analytic approximation⁴⁷ deviates by only a few percent from the numerical

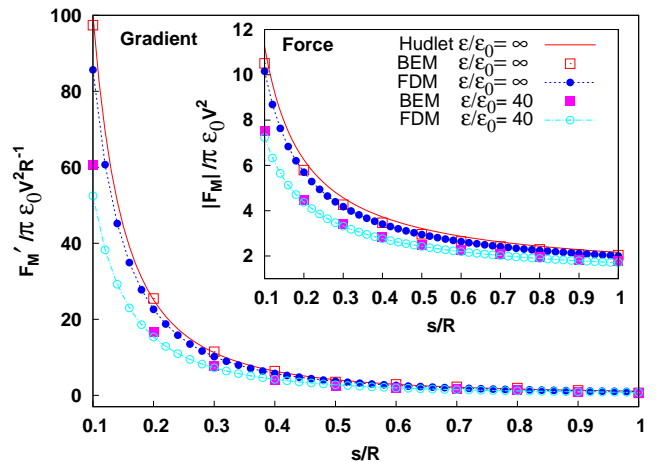


FIG. 4. (color online) Normalized macroscopic electrostatic force (inset) and force-gradient computed by our FDM versus the normalized tip separation s/R from a dielectric ($\epsilon/\epsilon_0 = 40.0$) and a conducting ($\epsilon/\epsilon_0 = \infty$) sample compared to BEM computations (Ref.⁴⁸), as well as to Hudlet's approximation (Ref.⁴⁷) in the second case (see text). The cantilever is absent, as assumed in those two treatments, but the remaining parameters are as described in the caption of Fig. 1.

results. In the following subsection we show that the contribution of the cantilever can be quite appreciable for a dielectric sample.

D. Results

The macroscopic electrostatic force and force-gradient versus the normalized tip-surface separation s/R for the system in Fig. 1 are shown in Fig. 5 for three different geometries: without, with a small and a large cantilever modelled as disks of thickness $0.5 \mu\text{m}$. The small disk radius is equal to the width of a typical rectangular AFM cantilever ($20 \mu\text{m}$) while the total area of the large disk (of radius $35 \mu\text{m}$) matches the area of the rectangular cantilever. The presence of the cantilever increases the capacitance and the electrostatic force. Because the cantilever is more than $10 \mu\text{m}$ away from the surface, its contribution to the force is often considered constant for tip-sample separations smaller than R , and therefore does not contribute to the force gradient. Our calculations [Fig. 5(a)] confirm that this is in fact true for a conductive sample. In this case, the main contribution to the force-gradient comes from the spherical cap, as can be seen from the solid line which corresponds to the analytic solution for a conducting spherical tip (see Appendix B). However, the conical shank of the tip and the cantilever affect the force at large separations, as shown in the inset and noticed earlier.^{33,34,47,50} On the other hand, if s/R is small, as shown in Fig. 5(b) and also emphasized in previous work^{51–53}, *over a thick dielectric sample both the*

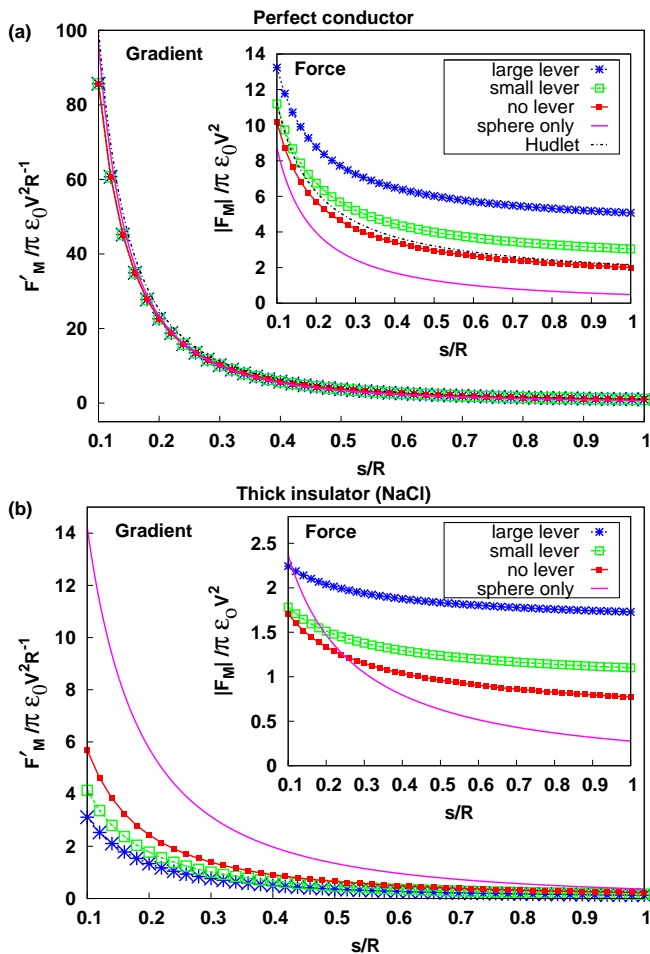


FIG. 5. (color online) Effect of the cantilever (size) on the macroscopic electrostatic force (inset) and force-gradient at different normalized tip separations from a conducting (a) and dielectric (b) sample. The cantilever is modelled as either a small or a large disk with radii of 20 and 35 μm , respectively. Other parameters are as in caption of Fig. 1. The solid lines show corresponding results for a tip approximated by a conducting sphere with radius $R = 20$ nm obtained by summing the analytic series for semi-infinite samples of both kinds (see Appendix B).

force and the force-gradient are significantly decreased, owing to field penetration into the sample.

A quantity of particular relevance in our multi-scale approach is the macroscopic electric field in the vacuum gap between the spherical tip end and the sample surface which polarizes the microscopic system. The variation of the electric field normalized to V/R at two points on the symmetry axis just below the tip and just above the surface is shown in Fig. 6 versus their normalized separation. The same quantities shown magnified in the inset for nanotip separations relevant for atomic-scale contrast, i.e. $z = s - h \lesssim 0.6$ nm, differ little and drop only weakly with increasing z . In the same distance range the z -

component of the electric field is two orders of magnitude stronger than the radial component parallel to the surface. These features are also clearly illustrated by the essentially equispaced horizontal equipotential contour lines in the vacuum region shown in the bottom inset of Fig. 1. This important observation greatly simplifies the desired coupling to atomistic calculations: we can consider the electric field E_z at the midpoint of the macroscopic tip-surface distance $s = z + h$ as a uniform external field acting on the isolated microscopic tip-sample system. The connection between those two scales is schematically illustrated in Fig. 7.

Figure 5 shows that for a conducting sample the force gradient can be accurately described by a spherical tip if $s < R$, although the force itself is increasingly underestimated at larger separations^{15,47}. In contrast, for a thick dielectric sample, the same description only provides the order of magnitude of F_M at small s/R , but exhibits a faster decrease with increasing separation and overestimates F'_M . Figure 6 reveals that a spherical model tip overestimates the electric field E_z under the tip at all separations, which then approaches V/R on the sphere (and zero on the surface) when $s \gg R$. This occurs because the induced surface charges can spread to the conical shank and the cantilever in the more realistic model. The contributions of those parts to the force F_M become nevertheless stronger than that of the sphere alone already at small s/R . In general, if $s/R \rightarrow 0$, the electric field under the tip, hence the force and the force gradient are enhanced owing to an increasingly localized surface polarization of both tip and sample, but remain finite if the sample is a dielectric, as explicitly demonstrated by the solution for a spherical tip (see Appendix B). Comparison with that solution (the solid curves in Fig. 5) shows that even at small separations contributions from both the conical shank and the cantilever contribute to the force, whereas mainly the conical shank affects the force gradient. Hence, ignoring those contributions causes an overestimation of the force-gradient if the sample is an insulator.

III. SHORT-RANGE ELECTROSTATIC FORCES

A. Evidence and previous models

When an AFM tip approaches a surface, short-range forces contribute to the tip-sample interaction and give rise to atomic-scale contrast in NCAFM. Hereafter, F_μ denotes the short-range force component perpendicular to the surface which can be extracted from measurements of Δf_1 vs. the closest tip approach distance d in an oscillation cycle.^{61,62} The contrast observed in V_{LCPD} in the same distance range cannot only be due to the long-range electrostatic force, but must be due to a short-range bias-dependent force. Arai and Tomitori were the first to infer the existence of such a force from $\Delta f_1(V_b)$

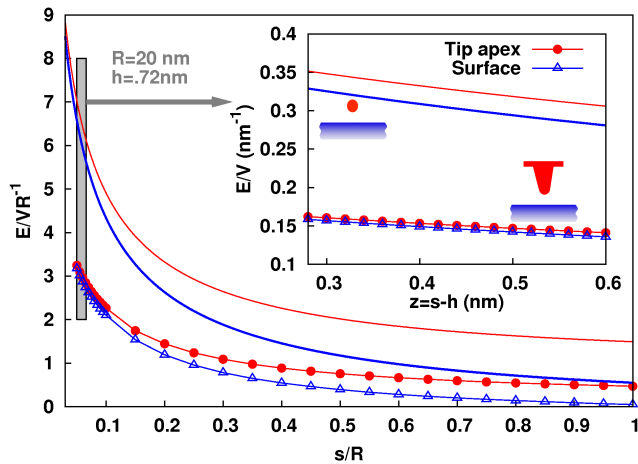


FIG. 6. (color online) Normalized macroscopic electric field just below the tip-apex and just above the dielectric sample surface ($\epsilon/\epsilon_0=5.9$) versus their normalized separation for the probe described in the caption of Fig. 1 (curves with symbols) and for a tip approximated by a conducting sphere of the same radius ($R = 20$ nm) (continuous curves). Inset: zoom into the range where atomic-scale contrast appears; the electric field between the tip and the surface changes by only a few percent and is hence nearly uniform.

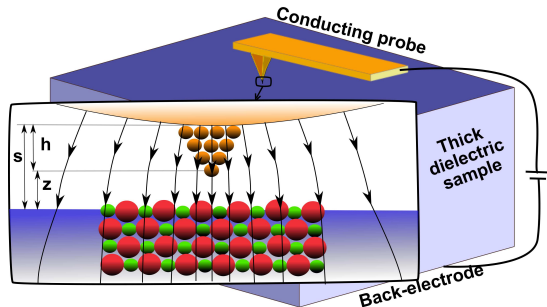


FIG. 7. (color online) Sketch of the AFM setup showing its macroscopic and microscopic parts on relevant scales. The macroscopic tip-sample separation is $s = z + h$, where h is the nanotip height and z is the nominal distance (without relaxation) between the apex atom and the surface. The macroscopic electric field \mathbf{E} obtained by solving Poisson's equation is applied as an external field to the atomistic subsystem shown in the zoom window. In the range $z < 0.6$ nm where atomic-scale contrast appears, the electric field in the vacuum gap can be considered to be uniform and equal to E_z at the mid-point $s/2$ on the symmetry axis.

curves recorded with a cleaned and sharpened silicon tip closer than 0.5 nm to a 7×7 reconstructed Si(111) surface.⁶³ In particular, above a Si adatom, they found a narrow peak growing with decreasing d superposed on the usual parabolic dependence around the plotted minimum of $-\Delta f_1(V_b)$ in their Fig. 1, i.e. for $V_b \simeq V_{CPD}$. Later the same authors pointed out that an even sharper peak appeared at the same bias in the simultaneously

recorded tunneling current.⁶⁴ This seemingly supported their original suggestion that the additional attractive force causing the peak in $-\Delta f_1(V_b)$ arose from the increased overlap due to the bias-induced energetic alignment of dangling bonds states localized at the tip apex and on Si surface adatoms. The formation of a covalent bond between those states has been shown to be responsible for the observed NCAFM contrast on the 7×7 reconstructed Si(111) surface.⁶⁵ In extensive recent measurements on the same system, however, Sadewasser et al reported parabolic $\Delta f_1(V_b)$ curves, but detected a rapid drop by about -1V followed by a gradual increase in V_{LCPD} above a Si adatom with decreasing d in the range where the extracted short-range force showed a similar behavior.¹⁶ The apparent discrepancy with respect to Arai and Tomitori's observations is not so surprising because tunneling is seldom observed with clean silicon tips, although it is routinely measured in STM, as well as in NCAFM on conducting and even semiconducting samples when using metal-coated silicon tips.^{66,67} An appreciable position- and distance-dependent tunneling current is, however, undesirable in dynamic atomic-scale LCPD measurements because it violates the basic assumption of an in-phase response to the AC voltage modulation by causing phase shifts which are difficult to compensate. This problem does not arise with insulating samples. Nevertheless, Arai and Tomitori's basic idea that bias-induced alignment of spatially localized surface states can lead to an enhanced site-dependent attractive force remains plausible even if a DC tunneling current cannot be sustained. Thus Krok and coworkers²⁷ suggested that the lower LCPD which they found across protruding In rows on the $c(2 \times 8)$ reconstructed InSb(001) surface was due to a bias-induced local electron transfer from a polar dangling bond on the electronegative Sb atom presumably picked by the Si tip to the nearest electropositive surface In atoms. The same authors also showed that the LCPD contrast between different lateral positions decays exponentially with increasing $d < 1$ nm.

Whereas bias-induced electron transfer is plausible for narrow-bandgap semiconductors like those previously mentioned, it is unlikely for overall neutral cleaved (001) surfaces of wide-bandgap insulators like alkali halides which neither have gap states, nor are reconstructed, but are only weakly rumped.⁶⁸ In Ref.²⁹ the atomic-scale LCPD contrast observed on KBr(001) was attributed to opposite surface cation and anion displacements in response to local electric fields induced by the macroscopic (in accordance with our definition) field. However, the authors approximated E_z by the electric field V/R at the surface of an isolated conducting spherical tip, the local unit cell polarizability by the bulk crystal (Clausius-Mosotti) expression, and neglected the macroscopic surface polarization. Although essentially constant on the scale of a nanometer-size nanotip, the latter, together with E_z is actually nonuniform on a lateral scale of order \sqrt{Rs} for separations $s \ll R$. They evaluated the macro-

scopic and microscopic surface charges densities σ_m and σ_μ induced on a conducting model tip by their E_z and by the displaced surface ions, respectively. Using Eq. (7) they computed the modulation of the electrostatic force. After further justified approximations, they obtained opposite LCPDs above cations and anions which *increased exponentially* with d . In a subsequent article,⁴² the same authors added a macroscopic force roughly representing the interaction of the cantilever with the back electrode, but still obtained a surprisingly large maximum in the absolute LCPD for $d \simeq 0.6$ nm. In a subsequent publication⁴³, even more reliable results were obtained for a cubic NaCl cluster partly embedded into a conducting sphere interacted with a NaCl(001) sample similar to ours via empirical shell-model potentials. Cluster ions inside the sphere were fixed and allowed to interact with the protruding cluster ions which thus formed a nanotip with a net charge $+e$ at the apex. The justification for such a model is that Si tips often pick up sample material and that simulations based on the same code produced reasonable results when compared to NCAFM measurements on alkali halides, e.g. on KBr(001).^{45,46} The results obtained can be considered representative of what is expected for a strongly polar tip interacting with an ionic crystal. Recently a simpler model for such a tip (conducting sphere terminated by a point charge or a point dipole) could account for the observed variation of the LCPD over a few nanometers.²²

Earlier studies mentioned that the short-range tip-sample interaction is bias-dependent but provided no recipe to investigate it theoretically. Moreover, they did not clarify how long-range and short-range bias-dependent forces are connected and the role of each in the observed KPFM signals. In the following sections we answer all of these questions and obtain and analyze in detail theoretical expressions for the site-dependent LCPD. Our approach is not limited to particular materials, but results are presented for the system described in the following Section which is representative of a neutral, but polarizable reactive clean Si tip interacting with an ionic crystal.

B. Density functional computations

As illustrated in Fig. 7 our microscopic system consists of a nanotip of height h protruding from the spherical end of the macroscopic tip and of a wider two-layer slab of sample atoms. Computations are performed within the local-density approximation to density functional theory (DFT) using norm-conserving HGH pseudopotentials⁶⁹ and the BigDFT package.⁷⁰ Relying on a wavelet basis set with locally adjustable resolution, this package calculates the self-consistent electron density, the total energy and its electrostatic component with selectable boundary conditions⁷¹ i.e. periodic in two directions and free in the third in our case. This allows us apply an external field perpendicular to the surface without artifacts

which can arise from periodic images in the z direction when using plane-wave of mixed basis sets. As already explained, the voltage biased macroscopic system determines the uniform electric field $E_z \propto V = V_b - V_{CPD}$ applied into the microscopic part (see Fig. 7). This provides the desired well-defined relationship between the bias-voltage and short-range forces which was lacking in previous approaches to LCPD contrast based on DFT computations.^{16,41}

Figure 8 illustrates the microscopic system used in the DFT computations reported here. The nanotip at the very end of a silicon tip is modelled as a cluster with a fixed (001) base of eight Si atoms with all dangling bonds passivated by H atoms in order to mimic the connection to the rest of the tip. The remaining Si atoms were pre-relaxed using the Minima Hopping Method⁷² previously employed to generate low-energy structures of silicon clusters and of similar model tips.⁷³ As in that work, the free Si atoms adopted a disordered configuration with several exposed under-coordinated atoms. In particular the protruding apex atom is threefold coordinated and hence has a dangling bond with a small dipole moment pointing towards the surface. As we verified, a distance five times the lattice constant of NaCl is large enough to get rid of the electrostatic interaction between this nano-tip and its images in the periodic directions. Therefore our sample consists of two 10×10 NaCl(001) layers containing 200 ions in total. For such a large system, we evidently perform calculations only at one single k-point, namely center of the surface Brillouin zone. With periodic boundary conditions applied along the main in-plane symmetry directions pre-relaxation of the sample only caused a small rumpling which preserved the basic periodicity of the truncated (001) surface. Although the silicon model tip and the sample were initially individually pre-relaxed, all tip and sample atoms were subsequently frozen in some of our KPFM simulations. In this way we could assess pure electronic polarization effects without effects due to the interaction-induced displacements of nuclei.

The silicon model tip was positioned so that its foremost atom was 0.65 nm above a sodium and chlorine surface ion, then moved towards the sample in steps of 0.02 nm. At each step the Kohn-Sham equations are solved iteratively. The topmost layer of the Si tip together with the passivating H atoms, as well as the bottom layer of the slab are kept fixed while other ions are free to relax until the Hellman-Feynman force exerted on each ion is less than 1 pN. This extremely tight tolerance is required only when the relative variation of the force when the bias changes is very small. The force F_μ exerted on the model tip is obtained by summing the z -components of the forces over atoms of the tip. Since the free atoms are well relaxed, their contribution to that force is not significant and was used as a measure of the error in forces. Figure 9 shows the microscopic force versus the tip-apex separation from Cl and Na surface sites without applied electric field. The same procedure

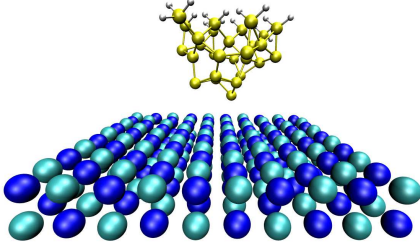


FIG. 8. (color online) The microscopic Si-tip NaCl-slab system used in our *ab initio* DFT calculations. The apex of a silicon AFM tip is modelled as a pre-relaxed $Si_{29}H_{18}$ cluster. All eight atoms in the top (001) layer are passivated by hydrogen atoms and kept fixed. The position of the foremost Si atom is (x, y, z) , z being the height from the surface. The model sample consists of two NaCl(001) layers each containing 10×10 ions with the bottom layer kept frozen. Periodic boundary conditions are applied along the x and y directions.

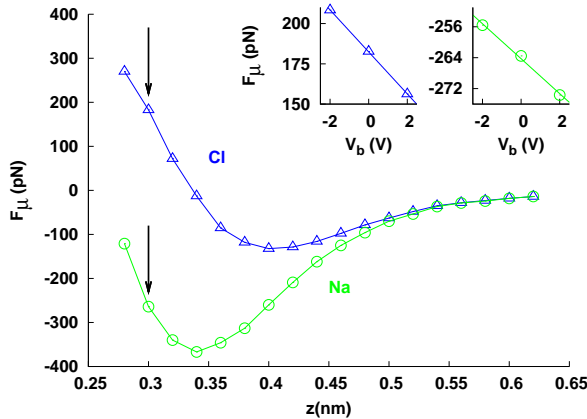


FIG. 9. (color online) Microscopic force on the Si nanotip above Na and Cl surface ions from *ab initio* calculations without an applied electric field. Insets: variation of the force as a function of the macroscopic bias voltage at a tip-surface separation of 0.30 nm. The error-bar (not shown) is $\sim 1pN$.

is repeated at each tip-sample separation for a few field strengths E_z determined as explained in subsection IID for effective biases $-2 \leq V = V_b - V_{CPD} \leq 2$ Volts applied to the macroscopic tip. For such biases and distances where F_μ becomes site-dependent, a nearly uniform macroscopic electric field of ~ 0.15 V/nm occurs in the vacuum gap, as discussed in Sec. II and illustrated in the inset of Fig. 6. No instabilities caused by electronic and/or atomic rearrangements appeared in that range of parameters. The variation of the force at the particular separation $z = 0.3$ nm is shown in the insets in Fig. 9. In contrast to the macroscopic capacitive force, *the short-range force depends linearly on the applied bias voltage*. As explained elsewhere,⁷⁴ this linear term arises from the interaction between distance-dependent but V -independent net charge densities on the tip and sample

surfaces with V -induced changes on the opposite surface and with the macroscopic electric field. Earlier studies obtained such a term by treating native ions or charged atoms adsorbed on the sample surface and/or the tip apex as point charges.^{22,23,29} Deviations from the linear behavior could occur for larger biases, especially near instabilities, as observed in computations for a charged nanotip.⁴³

The *basic quantity which determines the deviation of the LCPD from the background CPD* is the voltage-independent slope of the short-range force with respect to the applied voltage

$$a(x, y, z) = \frac{\partial}{\partial V} F_\mu(x, y, z; \mathbf{E}(V)). \quad (8)$$

As discussed in the Introduction, the background CPD is not a well-defined quantity for an insulator. For a real doped silicon tip-NaCl(001) sample, it would be different from the CPD of our microscopic system if charge equilibrium is achieved, as enforced by the self-consistency of the computations. Besides, no CPD is explicitly included in the description of the macroscopic system. Thus the effective bias $V = V_b - V_{CPD}$ would differ from that in a real system. Nevertheless, as long as this bias is in the Volt range, the slope a is unaffected.

Fig. 10(a) shows that the slope a exhibits a characteristic site-dependent distance dependence at separations less than 0.5 nm, and is larger above the more polarizable Cl ion. The underlying physics will be explained elsewhere.⁷⁴ The microscopic force-gradient F'_μ is also a linear function of bias voltage, and the distance-dependence of its slope $a'(x, y, z) = \partial F'_\mu / \partial V$, approximated to second order by linear interpolation between adjacent points on both sides of a given z -value, is shown in Fig. 10(c). Figures 10(b) and 10(d) show that a and a' are weaker if relaxation is allowed but that contrast appears below nearly the same distance and exhibits almost the same distance dependence. Thus, *for the assumed neutral Si nanotip, the contrast is mainly due to electronic polarization rather than to bias-induced ion displacements*.

In the approximation that the macro- and microscopic systems are coupled only through the macroscopic electric field, the z -component of the total force exerted on the tip is

$$F = F_M(s; V) + F_\mu(x, y, z; V) + F_{vdW}(s) \quad (9)$$

where $s = z + h$ and $V = V_b - V_{CPD}$. The long-range van der Waals force F_{vdW} is bias- and site-independent, being only a function of the mesoscopic geometry and is therefore henceforth ignored, although it affects the resonance frequency shift Δf in a NCAFM measurement. The macroscopic force F_M is capacitive ($\propto V^2$) while the microscopic force F_μ has been shown to be linear in V .

Three additional corrections couple the bias-dependent macro- and microscopic forces. The first correction $\delta C'V^2/2$ is due to an additional capacitive contribution caused by the presence of a polarizable nanoscale object in the gap between the macroscopic bodies. Owing to

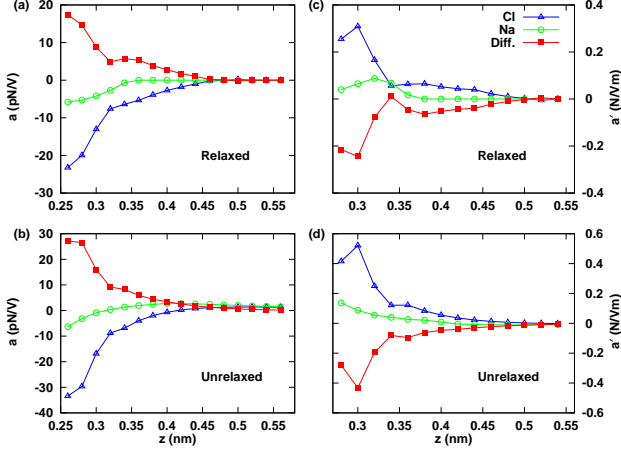


FIG. 10. (color online) Distance-dependence of the slopes $a = \partial F_\mu / \partial V$ and $a' = \partial F'_\mu / \partial V$ above Na and Cl surface ions with (a,c) and without (b,d) relaxation of the free atoms and ions during tip approach. The difference (contrast) between Na and Cl sites is shown by red (filled) symbols.

the small lateral dimensions of the nanotip compared to the radius of the macroscopic tip end, this correction is small,^{23,74} although it can become appreciable and site-dependent if the nanotip apex is charged.⁴³

The second correction arises only in that case or if the nanotip has a large net dipole moment⁷⁵. This leads to a site-independent LCPD with an approximate power-law approach towards a background CPD of several Volts. The interaction of the nanotip charge distribution with the macroscopic field \mathbf{E} could in principle be included in our description at separations s where \mathbf{E} can no longer be considered uniform. In that range, however, the charge or dipole might be approximated as point objects, as justified in the case of a conducting sample in the Supplementary Material of Ref.²². Because the charge or dipole are intrinsic, the interaction is proportional to V , so that this correction would give rise to long-range contributions to the slopes a and a' .^{22,23} In the case of our neutral Si nanotip, this correction is small.

The third correction arises because in reality the nanotip is in electrical contact with the macroscopic tip, so that the electron density at the interface differs from that near the top of our isolated silicon cluster. However, this model tip is large enough, so that the charge distribution near the apex, which dominates F_μ is not much affected, in contrast to models with smaller model tips. The self-consistently determined microscopic electric field between the nanotip apex and the sample surface differs from the applied macroscopic field E_z , but this effect is already included in the computed microscopic force.

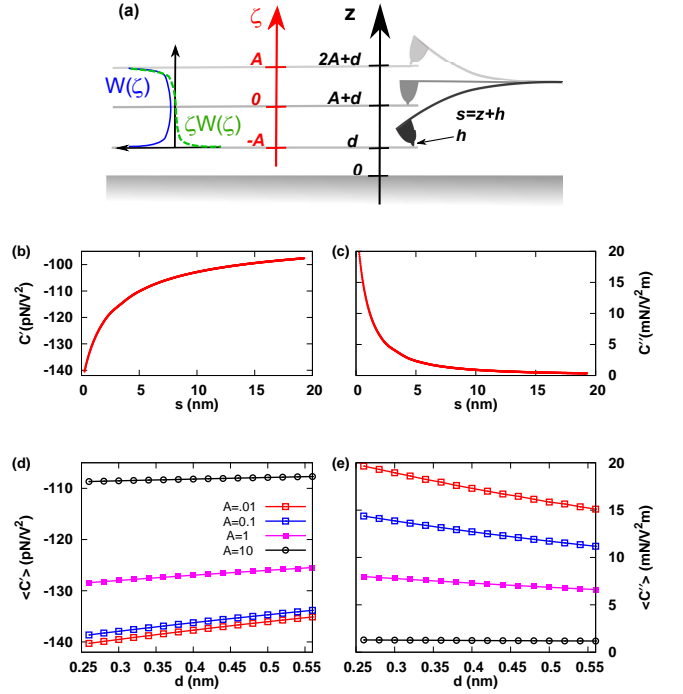


FIG. 11. (color online) (a) Sketch of the cantilever oscillating in its fundamental mode of a tip with finite amplitude A at the end. The weight functions used for calculating the cycle averages in Eqs. (16-17) are shown as functions of $\zeta = z - d - A$ where d is the closest tip apex-sample separation. Dependencies of the first (b) and second (c) spatial derivatives of the capacitance on the macroscopic separation $s = z + h$ calculated for the setup in Fig. 1, and of their cycle averages (d,e) on d for tip oscillation amplitudes $A = 0.01, 0.1, 1$ and 10 nm.

IV. AM AND FM KPFM SIGNALS AND LOCAL CONTACT POTENTIAL DIFFERENCES

A. Ultrasmall amplitude limit

The force gradient is more sensitive than the force to short-range interactions which are responsible for atomic-scale contrast in NCAFM and KPFM. Direct detection of the gradient is in principle possible if the variation of F_μ over the peak-to-peak oscillation amplitude is linear, e.g. if $2A$ is comparable to the spacing 0.02 nm of the computed points in Fig. 9. We first consider this simple limit which is commonly assumed in the KPFM literature, but is seldom achieved in NCAFM experiments. As explained in the Introduction, V_{LCPD} is operationally defined by nulling the KPFM signal generated by the force component F_ω at the modulation frequency. Assuming that the response V_{AC} is linear and instantaneous, $F_\omega = (dF/dV_b)V_{AC}$, and the deflection signal detected in AM-KPFM would be proportional to

$$F_\omega = [C'(z+h)(V_{DC} - V_{CPD}) + a(x,y,z)]V_{AC} \quad (10)$$

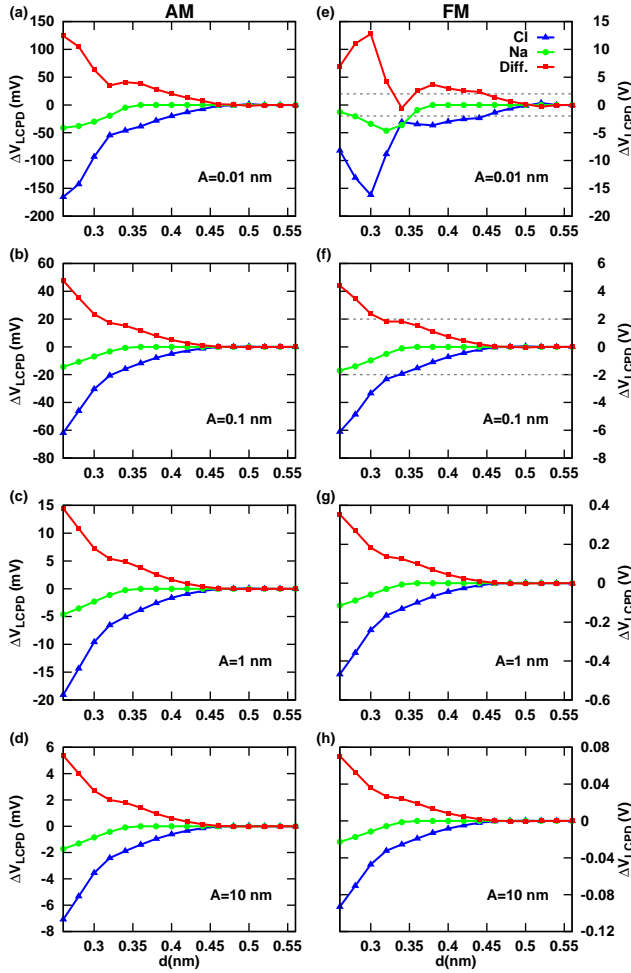


FIG. 12. (color online) Calculated deviations ΔV_{LCPD} for AM- (left column) and FM-KPFM (right column) versus closest tip apex-sample for tip oscillation amplitudes $A = 0.01$ nm (a,e), $A = 0.1$ nm (b,f), $A = 1$ nm (c,g), and $A = 1.0$ nm (d,h). In (e,f) the dashed horizontal lines indicate the range of validity of our DFT calculations (± 2 V).

in the ultrasmall amplitude limit, and would be nulled if

$$V_{DC} = V_{CPD} - \frac{a(x, y, z)}{C'(z+h)}. \quad (11)$$

Because the background V_{CPD} is not well-defined, and only $a(x, y, z)$ is site-dependent, we consider only the deviation of V_{LCPD} from V_{CPD} which is responsible for atomic-scale contrast, i.e.

$$\Delta V_{LCPD}^{AM} = -\frac{a(x, y, z)}{C'(z+h)}, \quad (12)$$

For a thick dielectric sample, as illustrated by Fig. 10(a) and by the points for $A=0.01$ nm in Fig. 11(d), the z -dependence of C' is weak over the range where $a(x, y, z)$ is appreciable ($s = z + h < 1$ nm). Therefore ΔV_{LCPD} differs from $a(x, y, z)$ by an essentially z -independent factor. Depending on the nanotip height h , this may no

longer hold in the case of a conductive sample or thin dielectric film on a conductive substrate.

In FM-KPFM the contribution of the modulated electrostatic force component F_ω to the frequency shift of the first resonant mode Δf_1 is detected and nulled. In the ultrasmall amplitude limit Δf_1 is proportional to the force-gradient¹⁰ and would therefore be nulled if

$$F'_\omega = [C''(z+h)(V_{DC} - V_{CPD}) + a'(x, y, z)]V_{AC} = 0.$$

The FM-counterpart of Eq. (12) is therefore

$$\Delta V_{LCPD}^{FM} = -\frac{a'(x, y, z)}{C''(z+h)}. \quad (13)$$

Again, as illustrated by Fig. 10(c) and by the points for $A=0.01$ nm in Fig. 11(e), the site- and distance dependence of this deviation is determined by $a'(x, y, z)$, but ΔV_{LCPD}^{FM} again differs from the numerator by an almost z -independent factor. The calculated LCPD deviations for $A = 0.01$ nm in the AM and FM modes are plotted in Figs. 12(a) and (e). Note that ΔV_{LCPD}^{FM} would be about hundred times stronger and would exceed the range of validity (± 2 V) of our DFT computations (limited between the horizontal lines in Figs. 12(e,f)), as well as the measured results in experiment, hence cannot be trusted. Therefore it is important to consider averaging over the range covered by the finite tip oscillation.

B. Finite amplitude expressions

In NCAFM with cantilevers the oscillation amplitude A is between several and a few tens of nanometers, so that the macroscopic capacitive electrostatic force can change by several orders of magnitude over an oscillation cycle. In practice, the detected AM and FM KPFM signals are given by differently weighted averages, namely³⁰

$$\langle F_\omega \rangle = \frac{1}{2\pi} \int_0^{2\pi} F_\omega [d + A(1 + \cos \phi)] d\phi$$

and⁷⁶

$$kA \frac{\langle \Delta f_\omega \rangle}{f} = -\frac{1}{2\pi} \int_0^{2\pi} F_\omega [d + A(1 + \cos \phi)] \cos \phi d\phi$$

where k is the flexural stiffness of the cantilever and $d = z_{min}$ is the closest tip apex-sample separation. Substituting the force from Eq. (10) and setting these averages to zero, one obtains

$$\Delta V_{LCPD}^{AM} = -\frac{\langle a(x, y, z) \rangle}{\langle C'(z+h) \rangle}, \quad (14)$$

$$\Delta V_{LCPD}^{FM} = -\frac{\langle a'(x, y, z) \rangle}{\langle C''(z+h) \rangle}, \quad (15)$$

where the cycle averages defined as

$$\begin{aligned}\langle g \rangle &\equiv \frac{1}{\pi} \int_{-A}^A W(\zeta) g(d + A + \zeta) d\zeta, \\ \langle g' \rangle &\equiv \frac{1}{\pi A} \int_{-A}^A \zeta W(\zeta) g(d + A + \zeta) d\zeta \\ &= \frac{1}{\pi A^2} \int_{-A}^A \sqrt{A^2 - \zeta^2} g'(d + A + \zeta) d\zeta\end{aligned}\quad (16)$$

$$(17)$$

depend both on d and A . As depicted in Fig. 11(a), $\zeta = z - (A + d)$ whereas $W(\zeta) = (A^2 - \zeta^2)^{-1/2}$ is a weight function with square root singularities at the turning points of the oscillation. The expression on the second line of Eq. (17) justifies the notation $\langle g' \rangle$ and shows that this quantity tends to $g'(d + A)$ when $A \rightarrow 0$, besides helping to relate the distance dependence of ΔV_{LCPD}^{FM} to those of $a'(x, y, z)$ and $C''(z + h)$. However, because $a(x, y, z)$ is computed with high precision, whereas $a'(x, y, z)$ is obtained by interpolation, we use the expression on the first line for numerical purposes. Furthermore, since $a(x, y, z)$ is known only at equispaced separations z_i where the DFT computations have been performed, the integrals in Eqs. (16-17) must be discretized. The adopted procedure, which deals with the singularities of the weight function $W(\zeta)$ at the integration limits,⁷⁷ is presented in Appendix C. There we also show that the discretized version of the expression in the first line of Eq. (17) reduces to the second order FD approximation of $g'(d + A)$ when $2A$ matches the spacing between adjacent z_i values, in accordance with the expression on the second line.

C. Results

Owing to the very different z -dependencies of $a(z)$ and $C'(z + h)$, shown respectively in Figs. 10(a) and 11(b), their cycle averages depend in different ways on d and A . The same holds for $a'(z)$ and $C''(z + h)$, shown respectively in Figs. 10(c) and 11(c). Figures 11(d) and 11(e) show the cycle averages of C' and C'' versus the closest tip-apex approach distance d for oscillation amplitudes $A = 0.01, 0.1, 1$ and 10 nm, whereas the cycle averages of V_{LCPD} calculated from Eqs. (14,15) are plotted in Fig. 12 for AM-KPFM (left column) and FM-KPFM (right column) for the same amplitudes in the range where $a(z)$ is finite. In that range, the cycle averages for $A = 0.01$ nm agree with the non-averaged quantities. Since the primary quantities were calculated at points spaced by 0.02 nm, this is not surprising in view of the remarks at the end of the preceding subsection. Thus, apart from small deviations introduced by the discretization procedure, the points in Figs. 12(a) and 12(e) which were actually calculated for $A = 0.01$ nm coincide with those given by Eqs.(12,13), and exhibit essentially the same distance dependencies as $a(d)$ and $a'(d)$, as already discussed in the subsection IV A.

Already above $A=0.1$ nm, however, the LCPD contrasts in both modes exhibit almost the same spatial de-

pendence as $a(d)$, although their respective magnitudes decrease if A is increased. Nevertheless, ΔV_{LCPD}^{FM} significantly exceeds ΔV_{LCPD}^{AM} ; this can be understood as follows. As seen in Figs. 11(d) and 11(e), $\langle C'' \rangle$ drops much faster than $-\langle C' \rangle$ if A is increased. As explained in the discussion of Fig. 5(b) this behavior reflects the increasing influence of the relative contributions of the tip shank and of the cantilever to $C'(z + h)$ in the range covered by the peak-to-peak oscillation. Especially $\langle C' \rangle$ is affected by the cantilever contribution which causes the very gradual levelling of $C'(z + h)$ apparent in Fig. 11(b). As seen in Fig. 11(c), this slowly varying contribution tends to cancel out in $C''(z + h)$, and, according to the second line in Eq. (17), in $\langle C'' \rangle$ as well.

On the other hand, $\langle a \rangle$ and $A\langle a' \rangle$ essentially coincide once a exceeds the range where a is noticeable. Indeed, the main contributions to those averages come from the vicinity of $z = d$ where the integrands in Eqs. (16) and (17) (first line) match. Expanding $W(\zeta)$ about this turning point, one finds that $\langle a \rangle \sim A^{-1/2}$ whereas $\langle a' \rangle \sim A^{-3/2}$, just like Δf_1 behaves in NCAFM.⁷⁶ According to Fig. 11(b,c) the same argument cannot be applied to $\langle C'' \rangle$ for $A \leq 10$ nm, and not at all to $\langle C' \rangle$ because $C'(s)$ varies only slowly up to $s = R = 20$ nm. Fig. 13 shows how the finite oscillation amplitude affects the relevant cycle averages, as well as ΔV_{LCPD} in the AM mode (left column) and in the FM mode (right column) at the closest tip apex-sample separation $d = 0.30$ nm indicated by arrows in Fig. 9.

The same trends persist at all separations $d < 0.5$ nm where LCPD contrast appears. $\langle a \rangle$ drops as $A^{-1/2}$, and $\langle a' \rangle$ drops as $A^{-3/2}$ already beyond $A = 0.1$ nm, while $\langle C' \rangle$ varies only little and $\langle C'' \rangle$ begins to drop somewhat slower than A^{-1} only above $A = 1$ nm. The resulting amplitude dependencies in both modes reflect the different dependencies of the numerators and denominators in Eqs. (14-15).

D. Discussion and Experimental Limitations

Expressions formally similar to Eqs. (14-15) were obtained by Nony *et al.*⁴² who also noticed that $\langle a \rangle$ and $A\langle a' \rangle$ almost coincide when A exceeds a few nanometers. However, their denominators came from a *short-range polarization contribution* $\propto V^2$ to the *microscopic force* F_μ rather than from the much larger capacitive force F_M . This results in a comparable ΔV_{LCPD} for AM and FM modes if A exceeds a few nanometers. However, by including the correct F_M and taking into account the different amplitude dependencies of the denominators in Eqs. (14-15), we conclude that the contrast should remain larger in the FM than in the AM mode for a given closest approach distance d and oscillation amplitude A . This prediction is independent of the particular system considered, but the mode-dependent signal to noise ratio must also be considered. Thus Kawai *et al.*³⁰ calculated the minimum detectable CPD as a function of A and

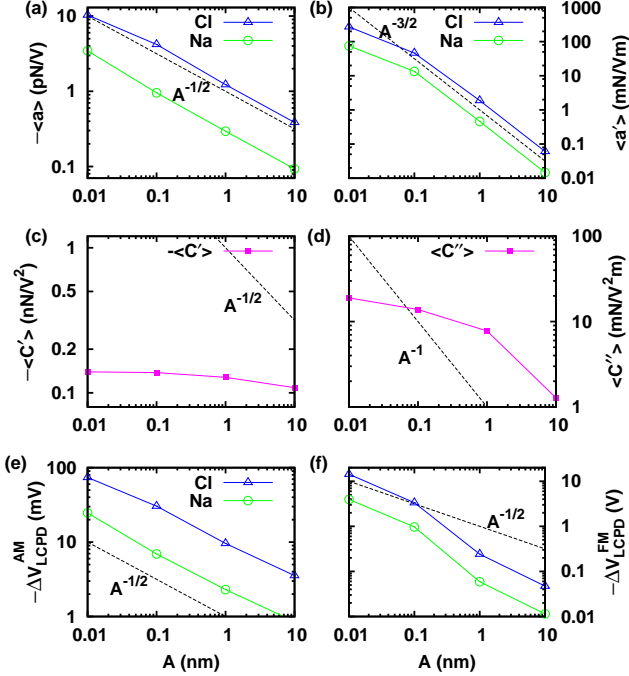


FIG. 13. (color online) Amplitude dependencies of the cycle averages $\langle a \rangle$ and $\langle a' \rangle$ (a,b), $\langle C' \rangle$ and $\langle C'' \rangle$ (c,d) and of the resulting deviations ΔV_{LCPD}^{AM} and ΔV_{LCPD}^{FM} (e,f) at a closest tip apex separation of $d=0.3$ nm above Cl and Na surface sites.

showed that it is smaller in the AM mode. Taking into account the discussions of Figs. 5 and 11, $\langle C' \rangle$ would be larger if the cantilever area is larger whereas $\langle C'' \rangle$ would be unaffected, whereas both quantities would be larger if the cone angle is broader or if the sample is a metal rather than an insulator, but $\langle C'' \rangle$ would be more strongly affected. On the other hand $\langle a \rangle$ and $\langle a' \rangle$ would be larger if the tip apex is charged⁴³ rather than neutral, or if the sample is a semiconductor with a reconstructed surface which exposes partially charged species like Si(111) 7×7 ^{16,30}. From this point of view the system studied here is especially challenging. Furthermore, the contrast ratio slowly decreases if A is increased, e.g. by a factor which drops from about 100 to 10 for oscillation amplitudes between 0.01 and 10 nm in our example.

For a meaningful comparison with NCAFM-KPFM measurements it is important to take *experimental limitations* into account. In view of the long-range LCPD variations due to surface and bulk inhomogeneities on real samples, one should compare computed atomic-scale LCPD variations with the difference between the LCPD measured at sub-nanometer separations d in the middle of a flat homogeneous island or terrace and the extrapolated long-range, essentially site-independent LCPD. This procedure would also suppress most of the long-range contributions to $\langle a \rangle$ and $\langle a' \rangle$ which would arise in the case of a charged or strongly polar tip²². More-

over, the comparison should be done with the same tip at constant d (slow distance control) because atomic-scale variations of d at constant $\Delta f_1(x, y, d)$ would induce such variations in the LCPD even if the latter is site-independent but has a different distance dependence as Δf_1 .

For the distance controller to function properly, Δf_1 must be chosen on the branch where this frequency shift becomes more negative if d is decreased. Furthermore, the maximum restoring force kA must be much larger than the maximum tip-sample attraction⁷⁶. For measurements with standard NCAFM cantilevers ($k \sim 20$ -40 N/m) this criterion is typically satisfied by using oscillation amplitudes $A > 5$ nm, and atomically resolved imaging is typically performed at distances $d \sim 0.4$ -0.5 nm. According to Fig. 12 the LCPD contrast which is then predicted to be 20-100 mV in the FM mode and a few mV in the AM mode approaches the experimental limits in both modes. Even if the AM-KPFM signal is enhanced by setting the modulation frequency at the second flexural resonance of the cantilever, the LCPD contrast predicted by our model would remain the same. This contrast would be stronger if the tip were charged. Unfortunately, available data showing atomic-scale contrast on (001) surfaces of NaCl and KBr is insufficient for a meaningful comparison between AM and FM KPFM. However, LCPD maps obtained with sputter-cleaned Si tips and similar measurement parameters on Si(111) 7×7 surfaces show that the contrast between Si adatoms and corner holes in the FM-mode¹⁶ is about ten times stronger than in the AM-mode³⁰. Moreover, data obtained from a direct determination of the maximum of Δf_1 versus bias voltage V_b agreed well with those obtained by nulling the FM-KPFM signal at the modulation frequency¹⁶.

The sizable LCPD contrast of several Volts predicted in the FM mode for amplitudes $A < 0.1$ nm should, however, be readily observable when using a tuning fork instead of a cantilever. Owing to the much higher stiffness $k \simeq 1800$ N/m of this deflection sensor, the above-mentioned criterion can be satisfied with such amplitudes close to the ultrasmall limit⁹. Combined NCAFM-KPFM measurements using such tuning forks with PtIr tips have only been done at low temperature by the time-consuming direct method mentioned in the Introduction.^{17,18} Unfortunately, no FM-KPFM measurements showing atomic-scale LCPD contrast on alkali halide (001) surfaces have so far been reported.

V. SUMMARY AND OUTLOOK

We proposed a general multiscale approach to compute electrostatic forces responsible for atomic-scale contrast in KPFM performed simultaneously with NCAFM. Although attention is focused on insulating samples and results are presented for a silicon tip interacting with a NaCl(001) sample, the approach is not restricted to particular sample or tip materials. The problem is split

into two parts coupled in a remarkably simple but novel fashion. First the electrostatic problem of the voltage-biased AFM probe (including the tip and the cantilever) against the grounded sample, treated as macroscopic perfect conductors or insulators, is solved by a finite-difference method with controlled accuracy on a non-uniform mesh. The method is capable of treating complex geometries with widely different dimensions, but is illustrated here for systems with cylindrical symmetry. The solution yields the electric potential and field distributions and the capacitance $C(s)$ of the system from which the electrostatic force F_M acting on the probe and its gradient are calculated as functions of the macroscopic tip-sample separation s . By comparing results obtained with and without the cantilever, as well as with the analytic solution for a tip approximated by a conducting sphere in Appendix B, *the contributions of the cantilever, the conical tip shank and of its spherical end can be recognized. If the sample is a thick insulator, all three affect the macroscopic force, whereas the last two affect the force gradient even at sub-nanometer separations relevant for atomic-scale contrast.*

Instead of the bias voltage V_b , the nearly uniform electric field obtained in that range is then applied as an external field to the microscopic part which can be treated by empirical atomistic or first principles methods. The *ab initio* BigDFT wavelet code employed here enables one to compute the short-range bias-dependent force on the tip apex represented by a cluster with an unprecedented accuracy of 1 pN per atom. For the Si-nanotip-NaCl(001) system considered here, this microscopic force F_μ is a linear function of the bias in the investigated range $V_b - V_{CPD} = \pm 2$ Volts. We argue that this is a general result, except close to atomic-scale instabilities caused by strong enough forces which could arise at very small separations and/or very large effective biases.

Adding the macroscopic and microscopic bias-dependent forces, expressions are obtained for the KPFM signals in the AM and the FM modes. The atomic-scale deviation ΔV_{LCPD} of the local CPD from its common value at large separations is the ratio of the derivatives $a = dF_\mu/dV_b$ and dC/ds averaged over the tip oscillation amplitude with different weights in AM- and FM-KPFM, as described by Eqs. (14-15). On the other hand, we explain the amplitude dependence of the atomic-scale LCPD contrast in both modes and predict that for typical amplitudes used in measurements with standard NCAFM cantilevers, this contrast should be much stronger in the FM mode. This is a consequence of the contributions of the cantilever and the tip shank to the KPFM signal in the AM mode, which are stronger on insulating samples. The same conclusion has previously been reached in comparisons of AM- and FM-KPFM measurements of long-range LCPD variations; such variations are caused by interactions of the biased probe with CPD inhomogeneities and surface charges on scales of several nanometers and above on conducting samples partly covered with ultrathin overlayers of different ma-

terials^{13,31}. However, the strong mode-dependent influence of distant contributions to dC/ds on the atomic-scale LCPD contrast has, to our knowledge, not been recognized because previous work on this topic assumed that only the tip apex mattered at sub-nanometer separations.

Because ΔV_{LCPD} depends on measurement parameters, it is desirable to *extract the more fundamental quantity* $a = dF_\mu/dV_b$ from combined KPFM measurements, just like the microscopic force F_μ is extracted from NCAFM measurements using, e.g. a widely accepted inversion algorithm⁶² or one based on the direct inversion of the discretized version of the first line of Eq.(15) described in Appendix C by back-substitution⁷⁷. Since ΔV_{LCPD} is predicted to be stronger in FM-KPFM, whereas its distance dependence is governed by the weighted average $\langle a' \rangle$ modes, the most appealing way to obtain $a(d)$ would be to extract a' then integrate it from the range where ΔV_{LCPD} vanishes down to the desired separation d . The averages $\langle a' \rangle$ and $\langle C'' \rangle$ can be separately obtained from direct measurements of the frequency shift Δf_1 as a function of bias¹⁶, namely from the shift of the maximum and the curvature of parabolic fits at several (x, y, d) positions. The signal/noise ratio of those averages can be improved by using AC modulation and lock-in detection at the modulation frequency. The averages could then be determined from the zero intercept V_{LCPD}^{FM} and the slope of the FM-KPFM signal $\langle \Delta f_\omega \rangle$ versus DC bias. An analogous procedure could be applied to determine $\langle a \rangle$ and $\langle C' \rangle$ from the AM-KPFM signal $\langle F_\omega \rangle$, then a itself by inversion, using suitably modified algorithms^{77,78}. Because the AM-KPFM signal/ratio is much superior if the modulation frequency f is at the second cantilever resonance³⁰, ΔV_{LCPD}^{AM} could be determined more accurately even if it is smaller than in FM-KPFM. In any case, note that the slope a reflects variations of the electrostatic potential outside the sample surface which are, however, locally enhanced by the proximity of the tip apex. Since the latter is in turn also polarized and deformed⁷⁹, a cannot simply be described as the convolution of the unperturbed electrostatic potential with a merely distance-dependent tip point-spread function, as in macroscopic electrostatics.³⁸

Complications due to averaging over the tip oscillation amplitude are to a certain extent avoided with tuning fork deflection sensors which enable direct measurements of $\langle \Delta f_\omega \rangle$ vs. bias, using amplitudes approaching the ultrasmall limit^{17,18}. Spectacular results have thus been obtained on isolated molecules adsorbed on a thin epitaxial NaCl(001) film by using tips with well-defined apex species stable at low temperature²¹. Most recently, V_{LCPD}^{FM} contrast reflecting changes in the intramolecular charge distribution has been observed upon a configurational switch triggered by a judiciously applied pulse⁸⁰. Our results shown in Figs. 12(e), 12(f) and 13(d) show that ΔV_{LCPD}^{FM} and a' still have a significant amplitude dependence between $A = 0.1$ and 0.01 nm, so that inversion is still necessary to obtain accurate results for typical

amplitudes used with tuning fork sensors.

Since such measurements use hard metal tips, while metal-coated tips are also used in NCAFM and/or KPFM measurements with cantilevers it would be desirable to develop appropriate nanotip models and to perform simulations like those described here. In particular, the recently fabricated sharp and stable W and Cr coated silicon tips^{67,75} and the stable atomic-scale resolution achieved with Cr-coated cantilevers at separations exceeding the usual range $d < 0.5$ nm merit further attention. Intentionally picked atoms or molecules at the apex would be worth studying in a further step. Another class of systems which merit further investigations involve silicon nanotips with a picked-up cluster of foreign material, NaCl in particular, which have so far been studied by DFT in the absence of a sample⁸¹ or represented by a cluster of the same material as the sample using empirical interaction potentials^{43,45}.

Note finally that all macroscopic probe models, including ours, provide a better description of metallic or metal-coated tips than of real silicon tips. Indeed, even if the native oxide is removed by sputtering, a silicon layer of few nanometers depleted of charge carriers still separates the tip surface from the highly doped conducting tip interior. Although it was taken into account in previous treatments of KPFM of semiconductor devices³, this depletion layer remains to be included when modelling Si tips, e.g. by allowing a smaller effective radius R of the equipotential at the applied bias voltage and a larger effective separation s from the sample surface.

ACKNOWLEDGMENTS

This work has been supported by the Swiss National Science Foundation (SNF) and the Swiss National Center of Competence in Research (NCCR) on Nanoscale Science. The CPU intensive computations were done at the Swiss National Supercomputing Center (CSCS) in Manno.

Appendix A: Sign of the macroscopic electrostatic force

Using the virtual work method, the macroscopic electrostatic tip-sample interaction can be calculated from the potential energy stored in the capacitor formed between the tip and the back-electrode. The (real) force acting on the tip F_z , which is considered constant during a virtual arbitrary infinitesimal tip displacement δz , performs a virtual work $\delta w = F_z \cdot \delta z = -\delta U$, where $U = U_c + U_b$ is the total energy of the system including contributions from both the capacitor and the biasing battery which maintains a fixed potential difference V between the both electrodes. In response to this displacement, the battery transfers a charge δQ between the electrodes in order to keep their potential difference fixed.

It costs a change of $\delta U_b = -\delta Q \cdot V$ in the energy of the battery. Whereas the energy of the capacitor changes by $\delta U_c = \frac{1}{2}\delta Q \cdot V$, which implies $U_b = -2U_c$, i.e.

$$\delta U = \delta U_c + \delta U_b = -\delta U_c.$$

The electrostatic force is therefore

$$F_z = -\frac{\delta U}{\delta z} = +\frac{\delta U_c}{\delta z} = +\frac{1}{2}\frac{\delta C}{\delta z}V^2$$

and is always attractive because $\delta C/\delta z < 0$.

Appendix B: Conducting sphere against a thick dielectric slab

The force between a conducting sphere of radius R at potential V facing a dielectric slab grounded on the bottom can be calculated by means of the image charge method. For a semi-infinite dielectric, we found that the solution is given by remarkably simple generalization of the treatment in section 5.08 of Smythe's textbook⁵⁸ for a semi-infinite conductor. Details, further analytic results and useful approximations, which are of general interest for scanning force microscopy, will be presented elsewhere.⁸² The potential Φ in the region between the sphere and the slab is generated by a series of point charges $\{q_n, z_n\}$ inside the sphere and their corresponding images $\{-\beta q_n, -z_n\}$ below the surface of the dielectric, where $\beta = (\epsilon - \epsilon_0)/(\epsilon + \epsilon_0)$, ϵ and ϵ_0 being the permittivities of the dielectric and of vacuum, respectively. The first charge $q_1 = 4\pi\epsilon_0VR$ is located at the center of the sphere $z_1 = R + s$. Physically, the image charges represent the effect of the polarization induced at the surface of the dielectric which causes a jump discontinuity in E_z . Together with the other charges they ensure that the sphere surface remains equipotential at V .

We find

$$q_n = q_1 \sinh \alpha \left(\frac{\beta^{n-1}}{\sinh n\alpha} \right), \quad (\text{B1})$$

where $\cosh \alpha = z_1/R$ and

$$z_n = R \sinh \alpha \coth n\alpha, \quad (\text{B2})$$

as in Smythe's treatment ($\beta = 1$). Except at the contact point ($s = 0$), the charges q_n decay exponentially fast towards zero and this solution provides convenient expressions for the capacitance $C(s) = q_{sph}/V$, where

$$q_{sph} = \sum_{n=1}^{\infty} q_n = 4\pi\epsilon_0RV \sinh \alpha \times \sum_{n=1}^{\infty} \frac{\beta^{n-1}}{\sinh n\alpha}, \quad (\text{B3})$$

and the z-component of the force $(dC/ds)V^2/2$

$$F_M = 2\pi\epsilon_0V^2 \sum_{n=2}^{\infty} \frac{\beta^{n-1}}{\sinh n\alpha} (\coth \alpha - n \coth n\alpha), \quad (\text{B4})$$

the force gradient dF_M/ds , and the electric field at $\rho = 0, z = 0$

$$E_z = \frac{V}{R} \frac{1 + \beta}{\sinh \alpha} \sum_{n=1}^{\infty} \frac{\beta^{n-1} \sinh n\alpha}{\cosh^2 n\alpha}. \quad (\text{B5})$$

These series have been used to evaluate the solid lines in Figs. 5 and 6(b). The truncation error can be reduced by generalizing a trick proposed for the conducting sphere-plane problem⁴⁴. If a series is truncated at some $n = k$, the remainder can be summed up analytically if one assumes $z_{n>k} \simeq z_{\infty} = R \sinh \alpha$. Thus, because $q_{n+1}/q_{n>k} \simeq \beta R/(z_1 + z_{\infty})$,

$$q_{\infty} \equiv \sum_{n=k+1}^{\infty} q_n \simeq \frac{q_{k+1}}{1 - \beta R/(z_1 + z_{\infty})} = \frac{q_{k+1}}{1 - \beta e^{-\alpha}}.$$

Adding the correction to the first 5 terms, q_{sph} is obtained with an accuracy of 10^{-5} for $\epsilon/\epsilon_0 = 5.9, s/R = 0.1$.

For an ideal conductor ($\beta = 1$) these expressions reduce to those of Smythe⁵⁸ and diverge in the limit $s \rightarrow 0$ (i.e. $\alpha \rightarrow 0$). In our case $\beta < 1$, and in the same limit the resulting series converge and can in fact be summed explicitly.⁸² The result for $F(s = 0)$ was given without proof in Eq. (2) of Ref.⁵¹. For NaCl ($\epsilon/\epsilon_0 = 5.9, \beta = 0.71$) one obtains limiting values of $C/\pi\epsilon_0 R = 6.98, F/\pi\epsilon_0 V^2 = -6.77$ (i.e. $F = -0.188$ nN/V² independent of sphere radius), $F'/\pi\epsilon_0 V^2 R^{-1} = 188.7$ and $E/VR^{-1} = 20.4$. In the case of a dielectric slab of finite thickness t , mirror images of all previously mentioned charges with respect to the grounded back-electrode must also be considered. They ensure that the field lines inside the dielectric become perpendicular to the grounded back-electrode instead of spreading radially. If $z_1 = R + s \ll t$, further images charges induced by those mirror charges can be neglected to order $\mathcal{O}((z_1/t)^2)$. Moreover, the electric force exerted by the mirror charges on the biased sphere can then be approximated as the Coulomb force between q_{sph} at its center and a lumped mirror charge $-(1 - \beta)q_{sph}$, $2(z_1 + t)$ away, i.e.

$$F_{add} \simeq \frac{-(1 - \beta) q_{sph}^2}{4\pi\epsilon_0 (2t)^2} = \pi\epsilon_0 V^2 \frac{2\epsilon_0}{\epsilon + \epsilon_0} \left(\frac{R}{t}\right)^2 \left(\frac{q_{sph}}{q_1}\right)^2.$$

For relevant values $s < R \sim 10$ nm and $t \sim 1$ mm, this correction is below $(R/t)^2/6.8 \sim 10^{-11}$ times the force

given by Eq. (B4), i.e. negligible in practice. A similar expression of comparable magnitude was proposed in Ref.⁴², but was erroneously assumed to represent F_M .

Appendix C: Discretized integrals for finite tip oscillation amplitudes

Assuming that $N + 1$ equispaced data points $\{z_i\}$ are sufficiently close together such that $g(z)$ remains almost constant within an interval length $\delta = 2A/N$, the integration in Eq. (16) can be approximated by a finite sum

$$\langle g(z) \rangle \simeq \frac{1}{\pi} \sum_{i=0}^N W_i g_i$$

where $g_i \equiv g(z_i)$ is either $g_i = a(z_i)$ or $g_i = C(z_i + h)$; Since $W(\zeta) = 1/\sqrt{A^2 - \zeta^2}$ we obtain

$$W_i = \int_{\zeta_i^-}^{\zeta_i^+} W(\zeta) d\zeta = \arcsin\left(\frac{\zeta_i^+}{A}\right) - \arcsin\left(\frac{\zeta_i^-}{A}\right)$$

where $\zeta_i^{\pm} = (i \pm \frac{1}{2})\delta - A$ are the midpoints between ζ_i and $\zeta_{i\pm 1}$. Taking into account the rapid variation of $W(\zeta)$ near the integration limits defined as $\zeta_0^- = -A$ and $\zeta_N^+ = A$, the square root singularities of $W(\zeta)$ at those turning points are approximately included with this modified trapezoid integration method. Sufficiently far from those points $W_i \simeq W(\zeta_i)\delta$ so that the standard trapezoid approximation is recovered. The analogous approximation for Eq.(17) namely

$$\langle g'(z) \rangle \simeq \frac{1}{\pi} \sum_{i=0}^N W_i^* g_i$$

involves⁷⁷

$$W_i^* = \frac{1}{A} \int_{\zeta_i^-}^{\zeta_i^+} \zeta W(\zeta) d\zeta = \sqrt{1 - \left(\frac{\zeta_i^-}{A}\right)^2} - \sqrt{1 - \left(\frac{\zeta_i^+}{A}\right)^2}.$$

Note that in the $A \rightarrow 0$ limit only the data points at the two limits are taken into account. Indeed, if $N = 1, A = \delta/2$ and $W_0 = W_1$, hence $\langle g \rangle = (g_0 + g_N)/2$, and $W_0^* = -W_1^*$, hence $\langle g' \rangle = (g_N - g_0)/2A$, so that Eqs. (14,15) consistently approximate the corresponding zero-amplitude equations, Eqs. (12,13). Similarly, if $N=2, A = \delta$ and one obtains $W_0 = W_2, W_1 = 0$ and $W_0^* = -W_2^*, W_1^* = 0$ and Eqs. (12,13) are again recovered.

¹ J. Weaver and D. Abraham, J. Vac. Sci. Technol. B **9**, 1559 (1991)

² M. Nonnenmacher, M. O'Boyle, and H. Wickramasinghe, Appl. Phys. Lett. **58**, 2921 (1991)

³ S. Sadewasser, T. Glatzel, M. Rusu, A. Jager-Waldau, and M. C. Lux-Steiner, Appl. Phys. Lett. **80**, 2979 (2002)

⁴ C. Barth, A. S. Foster, C. R. Henry, and A. L. Shluger, Advanced Materials **23**, 477 (2011)

- ⁵ S. Sadewasser and T. Glatzel, *Kelvin Probe Force Microscopy: Measuring and Compensating Electrostatic Forces* (Springer, Heidelberg Dordrecht London New York, 2011)
- ⁶ F. E. Olsson and M. Persson, *Surf. Sci.* **540**, 172 (2003)
- ⁷ C. Barth and C. R. Henry, *Phys. Rev. Lett.* **98**, 136804 (2007)
- ⁸ F. J. Giessibl, *Science* **267**, 68 (1995)
- ⁹ F. J. Giessibl, *Rev. Mod. Phys.* **75**, 949 (2003)
- ¹⁰ T. R. Albrecht, P. Grütter, D. Horne, and D. Rugar, *J. Appl. Phys.* **69**, 668 (1991)
- ¹¹ A. Kikukawa, S. Hosaka, and R. Imura, *Rev. Sci. Instrum.* **67**, 1463 (1996)
- ¹² S. Kitamura and I. M., *Appl. Phys. Lett.* **72**, 3154 (1998)
- ¹³ U. Zerweck, C. Loppacher, T. Otto, S. Graftröm, and L. M. Eng, *Phys. Rev. B* **71**, 125424 (2005)
- ¹⁴ F. J. Giessibl, *Appl. Phys. Lett.* **73**, 3956 (1998)
- ¹⁵ M. Guggisberg, M. Bammerlin, C. Loppacher, O. Pfeiffer, A. Abdurixit, V. Barwich, R. Bennewitz, A. Baratoff, E. Meyer, and H.-J. Güntherodt, *Phys. Rev. B* **61**, 11151 (2000)
- ¹⁶ S. Sadewasser, P. Jelinek, C.-K. Fang, O. Custance, Y. Yamada, Y. Sugimoto, M. Abe, and S. Morita, *Phys. Rev. Lett.* **103**, 266103 (2009)
- ¹⁷ T. König, G. H. Simon, H.-P. Rust, and M. Heyde, *J. Phys. Chem. C* **113**, 11301 (2009)
- ¹⁸ L. Gross, F. Mohn, P. Liljeroth, J. Repp, F. J. Giessibl, and G. Meyer, *Science* **324**, 1428 (2009)
- ¹⁹ H. Diesinger, D. Deresnes, J. Nys, and T. Mélin, *Ultramicroscopy* **108**, 773 (2008)
- ²⁰ C. Sommerhalter, T. W. Matthes, T. Glatzel, A. Jäger-Waldau, and M. C. Lux-Steiner, *Appl. Phys. Lett.* **75**, 286 (1999)
- ²¹ L. Gross, F. Mohn, N. Moll, P. Liljeroth, and G. Meyer, *Science* **325**, 1110 (2009)
- ²² C. Barth, T. Hynninen, M. Bielecki, C. R. Henry, A. S. Foster, F. Esch, and U. Heiz, *New J. Phys.* **12**, 093024 (2010)
- ²³ F. Bocquet, L. Nony, and C. Loppacher, *Phys. Rev. B* **83**, 035411 (2011)
- ²⁴ S. Kitamura, K. Suzuki, M. Iwatsuki, and C. Mooney, *Appl. Surf. Sci.* **157**, 222 (2000)
- ²⁵ K. Okamoto, Y. Sugawara, and S. Morita, *Appl. Surf. Sci.* **188**, 381 (2002)
- ²⁶ K. Okamoto, K. Yoshimoto, Y. Sugawara, and S. Morita, *Appl. Surf. Sci.* **210**, 128 (2003)
- ²⁷ F. Krok, K. Sajewicz, J. Konior, M. Goryl, P. Piatkowski, and M. Szymonski, *Phys. Rev. B* **77**, 235427 (2008)
- ²⁸ G. H. Enevoldsen, T. Glatzel, M. C. Christensen, J. V. Lauritsen, and F. Besenbacher, *Phys. Rev. Lett.* **100**, 236104 (2008)
- ²⁹ F. Bocquet, L. Nony, C. Loppacher, and T. Glatzel, *Phys. Rev. B* **78**, 035410 (2008)
- ³⁰ S. Kawai, T. Glatzel, H.-J. Hug, and E. Meyer, *Nanotechnology* **21**, 245704 (2010)
- ³¹ T. Glatzel, S. Sadewasser, and M. Lux-Steiner, *Appl. Surf. Sci.* **210**, 84 (2003)
- ³² T. Glatzel, L. Zimmerli, S. Koch, B. Such, S. Kawai, and E. Meyer, *Nanotechnology* **20**, 264016 (2009)
- ³³ T. Hochwitz, C. Henning, A. K. ND Levey, C. Daghljan, and J. Slinkman, *J. Vac. Sci. Technol. B* **14**, 457 (1996)
- ³⁴ H. O. Jacobs, P. Leuchtman, O. J. Homan, and A. Stemmer, *J. Appl. Phys.* **84**, 1168 (1998)
- ³⁵ S. Belaidi, F. Lebon, P. Girard, G. Leveque, and S. Pagano, *Appl. Phys. A* **66**, S239 (1998)
- ³⁶ J. Colchero, A. Gil, and A. M. Baró, *Phys. Rev. B* **64**, 245403 (2001)
- ³⁷ S. Gómez-Moñivas, L. S. Froufe, R. Carminati, J. J. Grefet, and J. J. Sáenz, *Nanotechnology* **12**, 496 (2001)
- ³⁸ E. Strassburg, A. Boag, and Y. Rosenwaks, *Rev. Sci. Instrum.* **76**, 083705 (2005)
- ³⁹ J. Konior, *J. Appl. Phys.* **101**, 084907 (2007)
- ⁴⁰ Y. Shen, D. M. Barnett, and P. M. Pinsky, *Rev. Sci. Instrum.* **79**, 023711 (2008)
- ⁴¹ A. Masago, M. Tsukada, and M. Shimizu, *Phys. Rev. B* **82**, 195433 (2010)
- ⁴² L. Nony, F. Bocquet, C. Loppacher, and T. Glatzel, *Nanotechnology* **20**, 264014 (2009)
- ⁴³ L. Nony, A. S. Foster, F. Bocquet, and C. Loppacher, *Phys. Rev. Lett.* **103**, 036802 (2009)
- ⁴⁴ L. Kantorovich, A. Foster, A. Shluger, and A. Stoneham, *Surf. Sci.* **445**, 283 (2000)
- ⁴⁵ R. Hoffmann, L. N. Kantorovich, A. Baratoff, H. J. Hug, and H.-J. Güntherodt, *Phys. Rev. Lett.* **92**, 146103 (2004)
- ⁴⁶ K. Ruschmeier, A. Schirmeisen, and R. Hoffmann, *Phys. Rev. Lett.* **101**, 156102 (2008)
- ⁴⁷ S. Hudlet, M. Saint Jean, C. Guthmann, and J. Berger, *Eur. Phys. J. J.* **2**, 5 (1998)
- ⁴⁸ Y. Shen, D. M. Barnett, and P. M. Pinsky, *Eng. Anal. Bound. Elem.* **32**, 682 (2008)
- ⁴⁹ J. D. Jackson, *Classical Electrodynamics* (Wiley, New York, 2001)
- ⁵⁰ S. Belaidi, P. Girard, and G. Leveque, *J. Appl. Phys.* **81**, 1023 (1997)
- ⁵¹ S. Gómez-Moñivas, L. S. Froufe-Pérez, A. J. Caamaño, and J. J. Sáenz, *Appl. Phys. Lett.* **79**, 4048 (2001)
- ⁵² G. M. Sacha, E. Sahagún, and J. J. Sáenz, *J. Appl. Phys.* **101**, 024310 (2007)
- ⁵³ G. M. Sacha and J. J. Sáenz, *Appl. Phys. Lett.* **85**, 2610 (2004)
- ⁵⁴ G. Elias, T. Glatzel, E. Meyer, A. Schwarzman, A. Boag, and Y. Rosenwaks, *Beilstein J. Nanotechnol.* **2**, 252 (2011)
- ⁵⁵ S. Sadewasser, T. Glatzel, R. Shikler, Y. Rosenwaks, and M. Lux-Steiner, *Appl. Surf. Sci.* **210**, 32 (2003)
- ⁵⁶ G. Valdrè and D. Moro, *Nanotechnology* **19**, 405502 (2008)
- ⁵⁷ D. S. H. Charrier, M. Kemerink, B. E. Smalbrugge, T. de Vries, and R. A. J. Janssen, *ACS Nano* **2**, 622 (2008)
- ⁵⁸ W. R. Smythe, *Static and dynamic electricity*, 2nd ed. (McGraw-Hill, New York, 1950) Chap. 5
- ⁵⁹ O. Schenk, A. Wächter, and M. Hagemann, *Comput. Optim. Appl.* **36**, 321 (2007), www.pardiso-project.org
- ⁶⁰ <http://pages.unibas.ch/comphys/comphys/software>
- ⁶¹ U. Dürig, *Appl. Phys. Lett.* **75**, 433 (1999)
- ⁶² J. E. Sader and S. P. Jarvis, *Appl. Phys. Lett.* **84**, 1801 (2004)
- ⁶³ T. Arai and M. Tomitori, *Phys. Rev. Lett.* **93**, 256101 (2004)
- ⁶⁴ T. Arai and M. Tomitori, *Phys. Rev. B* **73**, 073307 (2006)
- ⁶⁵ M. A. Lantz, H. J. Hug, R. Hoffmann, P. J. A. van Schendel, P. Kappenberger, S. Martin, A. Baratoff, and H.-J. Güntherodt, *Science* **291**, 2580 (2001)
- ⁶⁶ Y. Sugimoto, Y. Nakajima, D. Sawada, K. Morita, M. Abe, and S. Morita, *Phys. Rev. B* **81**, 245322 (2010)
- ⁶⁷ Y. Kinoshita, Y. Naitoh, Y. J. Li, and Y. Sugawara, *Rev. Sci. Instrum.* **82**, 113707 (2011)
- ⁶⁸ F. W. de Wette, W. Kress, and U. Schröder, *Phys. Rev. B* **32**, 4143 (1985)

- ⁶⁹ C. Hartwigsen, S. Goedecker, and J. Hutter, Phys. Rev. B **58**, 3641 (1998)
- ⁷⁰ L. Genovese, A. Neelov, S. Goedecker, T. Deutsch, S. A. Ghasemi, A. Willand, D. Caliste, O. Zilberberg, M. Rayson, A. Bergman, and R. Schneider, J. Chem. Phys. **129**, 014109 (2008)
- ⁷¹ L. Genovese, T. Deutsch, A. Neelov, S. Goedecker, and G. Beylkin, J. Chem. Phys. **125**, 074105 (2006)
- ⁷² S. Goedecker, J. Chem. Phys. **120**, 9911 (2004)
- ⁷³ S. A. Ghasemi, S. Goedecker, A. Baratoff, T. Lenosky, E. Meyer, and H. J. Hug, Phys. Rev. Lett. **100**, 236106 (2008)
- ⁷⁴ A. Sadeghi, A. Baratoff, and S. Goedecker, unpublished
- ⁷⁵ G. Teobaldi, K. Lämmle, T. Trevethan, M. Watkins, A. Schwarz, R. Wiesendanger, and A. L. Shluger, Phys. Rev. Lett. **106**, 216102 (2011)
- ⁷⁶ F. J. Giessibl, Phys. Rev. B **56**, 16010 (1997)
- ⁷⁷ O. Pfeiffer, *Quantitative dynamische Kraft- und Dissipationsmikroskopie auf molekularer Skala*, Ph.D. thesis, Basel University, Basel, Switzerland (2004)
- ⁷⁸ J. E. Sader and Y. Sugimoto, Appl. Phys. Lett. **97**, 043502 (2010)
- ⁷⁹ S. Kawai, T. Glatzel, S. Koch, A. Baratoff, and E. Meyer, Phys. Rev. B **83**, 035421 (2011)
- ⁸⁰ F. Mohn, L. Gross, N. Moll, and G. Meyer, Nature Nanotech., (2012), 10.1038/nnano.2012.20
- ⁸¹ M. Amsler, S. A. Ghasemi, S. Goedecker, A. Neelov, and L. Genovese, Nanotechnology **20**, 445301 (2009)
- ⁸² A. Sadeghi, A. Baratoff, and S. Goedecker, unpublished